Supporting Information

Associating Co single atoms with RuO_2 nanoparticles anchor on nitrogen-doped ultrathin porous carbon nanosheets as effective bifunctional oxygen electrocatalysts for rechargeable Zn-air batteries

Xuena Ma,[a] Mingyang Liu,*[a] Qi Li,[a] Xudong Xiao,[a] Jianan Liu,[a] Xiaoqin Xu,[a] Yihang Yin,[a], Panzhe Qiao,[b] Luoming Zhang,[a] Xiaoyan Zou,*[a] Ruihong Wang,*[a] and Baojiang Jiang*[a]

[a] Key Laboratory of Functional Inorganic Material Chemistry, Ministry of Education of the People's Republic of China, School of Chemistry and Materials Science, Heilongjiang University, Harbin 150080, P. R. China.

[b] Shanghai Synchrotron Radiation Facility, Shanghai Advanced Research Institute, Chinese Academy of Sciences, Shanghai, 201204 P. R. China.

Corresponding author (s):

* Mingyang Liu, Ruihong Wang, Baojiang Jiang.

Xuefu Road 74#, Wangang District, Harbin, 150080, China.

E-mail: jbj@hlju.edu.cn; wangruihong@hlju.edu.cn; zxy_18889@126.com;

lmy_0202@163.com (M. Y. Liu).

1. Experimental details

1.1. Material characterizations

In our study, the crystal phases of samples prepared at each step were investigated by X-ray powder diffractometer (XRD, Rigaku D/max 2500 diffractometer) using Cu Kα radiation (k = 1.5406A, 40 kV, 20 mA) at step scan of 0.02°. Raman spectra were obtained using a Renishaw UV-1000 Photon Design spectrometer at 532 nm excitation focused through a 100× microscope objective for a total interrogation spot size of ~1 μm. The morphology and microstructure of the samples were investigated by a Scanning electron microscope (SEM, S-4800 (Japan)) equipped with energy dispersive spectrometry (EDS). Brunauer-Emmett-Teller (BET) method and Barrett-Joyner-Halenda (BJH) theory were used to analyze the specific surface area and pore size distribution (PSD), respectively. Transmission electron microscopy (TEM) and high-resolution TEM (HRTEM) images were taken by a JEM-2100 electron microscope (JEOL) with an accelerating voltage of 200 kV. N_2 adsorption/desorption isotherms were obtained on a JW-BK112 at 77 K. The X-ray photoelectron spectroscopy (XPS) (Kratos-AXIS UL TRA DLD, AlKα X-ray source) observations were conducted to analyze the surface composition of the sample. The d-band center (εd) as derived from valence band spectra is given by $\varepsilon d = \int R(\varepsilon)\varepsilon d\varepsilon / \int R(\varepsilon)d\varepsilon$ are added in the revised supporting information [1]. Inductively coupled plasma optical emission spectroscopy (ICP-OES) was used to confirm the compositions of the samples.

1.2. Electrochemical measurements

Electrochemical measurements were conducted using an electrochemical workstation with the typical three-electrode system (CHI760E, Chenhua, Shanghai). The working electrode was a glassy carbon electrode (GCE, 4 mm) coated with the prepared electrocatalysts, while the reference

electrode was a saturated calomel electrode (SCE, +0.2438 V vs. standard hydrogen electrode, 3.0 M KCl) and the counter electrodes was a Pt wire. All of the potentials were converted to the reversible hydrogen electrodes (RHE). The recorded potentials were calibrated to RHE using the following Equations (1):

$$E_{RHE} = E_{SCE} + 0.2438 + 0.0592 \times pH \quad (1)$$

in which E_{RHE} and E_{SCE} represent the potentials relative to the RHE and SCE, respectively [2, 3]. The electrocatalysts ink was obtained by ultrasonically dispersing 5 mg of the as-prepared electrocatalyst in the mixture solution of 50 μL of 5 wt.% Nafion (Aldrich) and 100 μL of ethanol for 30 min. Then the electrocatalyst ink was evenly dripped onto a GCE. For ORR, LSV curves was performed in the alkaline medium of pH = 13 (0.1 M KOH) with the scan speed of 5 $mV \cdot s^{-1}$ under 1600 rpm. And for OER the polarization curves were recorded in the alkaline medium of pH = 13 (0.1 M KOH) with a scan rate of 2 $mV \cdot s^{-1}$ at room temperature. Commercial Pt/C (20 wt.% Pt, on Vulcan carbon black, Hesen Electric Co. Ltd, Shanghai, China) was used as a reference for all of the tests.

1.3. ORR activity measurements

Cyclic voltammetry (CV) tests were cycled positively in 0.1 M KOH solution at a scan rate of 0.05 V s^{-1} (0 to 1.2 V). Linear sweep voltammetry (LSV) tests were conducted in an O_2-saturated 0.1 M KOH solution at a scan rate of 0.001 V s^{-1} (0 to 1.2V) at a rotation rate of 1600 rpm. Chronoamperometry (CA), accelerated durability test (ADT), electrochemical impedance spectroscopy (EIS), and Tafel tests were performed using the reported methods. In addition, an important parameter for evaluating OER activity is the Tafel slope b, and the corresponding Tafel plots are constructed based on the LSV curves. Determined by the following Tafel Equation 2:

$$\eta = a + b\log|J| \quad (2)$$

Where η is the overpotential, b is the Tafel slope, and J is the current density

Rotating disk electrode (RDE) measurements were carried out in an O_2-saturated electrolyte at a scan rate of 0.001 V s^{-1} with the rotation rates from 400 to 2500 rpm. The Koutecky-Levich (K-L) plots (J^{-1} vs $\omega^{-1/2}$) were acquired in the potential range from 0.3 to 0.6 V from the RDE results, which could determine the electron transfer numbers (n), as shown in the following Equations 3 and 4:

$$\frac{1}{j} = \frac{1}{j_L} + \frac{1}{j_K} = \frac{1}{B\omega^{1/2}} + \frac{1}{nFkC_O} \quad (3)$$

$$B = 0.62nFC_0D_0^{2/3}v^{-1/6} \quad (4)$$

where, j was the apparent current density, j_K was the kinetic current density, j_L was the diffusion-limiting current density, ω was the angular velocity of the working electrode, n was the electron transfer number, F was the Faraday constant (96485 C mol^{-1}), C_0 was the bulk concentration of O_2 (1.2×10^{-6} mol cm^{-3}), D_0 was the diffusion coefficient of O_2 in electrolytes (1.9×10^{-5} cm^2 s^{-1}), and ν was the kinematic viscosity (0.01 cm^2 s^{-1}).

Rotating ring disk electrode (RRDE) measurements were conducted at an electrode rotation speed of 1600 rpm with a scan rate of 0.001 V s^{-1}. A constant ring potential was controlled at 0.5 V in O_2-saturated 0.1 M KOH solution. The electron transfer number (n) and the hydrogen peroxide yield [H_2O_2 (%)] were obtained from RRDE voltammograms, determined by the following Equations 5 and 6:

$$n = 4 \times \frac{I_d}{I_d + (I_r/N)} \quad (5)$$

$$H_2O_2\% = 200 \times \frac{I_r/N}{I_d + (I_r/N)} \quad (6)$$

Where I_d and I_r were the disk current and the ring current, respectively; N was H_2O_2 collection efficiency of the Pt ring with the value of 0.37.

1.4. OER activity measurements

OER tests were performed in 0.1 M KOH electrolyte solution. Linear sweep voltammetry (LSV) was carried out at a scan rate of 2 mV s^{-1} for the polarization curves, without iR-compensation correction [4-7]. The durability of catalyst after 10000 CV cycles was studied by using the accelerated durability test (ADT). EIS tests were performed at 1.58 V vs. RHE with frequencies ranging from 100 kHz to 100 MHz [8,9]. The electrochemically active area was calculated from the electrical double layer capacitance measurements, which were cycled at scan rates of 40, 60, 80, 100, and 120 mV s^{-1} with a potential range from 0.96 to 1.06 V vs. RHE. Tafel and CA tests were performed using the reported methods.

Moreover, one of the genuine approaches for electrochemical active sites measurement is the electrochemical surface area calculation via electrical double-layer capacitance (C_{dl}) using cyclic voltammetry (CV) [10-12]. Which are converted to ECSA according to the following Equations 7:

$$ECSA = C_{dl}/C_s \quad (7)$$

The specific capacitance (Cs) value Cs=0.040 mF cm^{-2} in 0.1 M KOH is adopted from previous reports.

1.5. Fabrication of home-made Zn-air batteries

The primary battery was designed at room temperature with an oxygen-saturated 6.0 M KOH solution containing 0.2 M Zn $(Ac)_2$ as electrolyte, using a polished Zn plate as the anode and the

composite substrates (hydrophobic carbon paper + waterproof membrane + nickel foam) produced in Changsha Spring New Energy Technology Co., Ltd as the catalyst carrier of the air electrode. Catalyst ink was prepared by mixing 50 μL of 5 wt.% Nafion (Aldrich), 1 mL of ethanol and 5 mg Co_{SA}-RuO_2-NUCN powder, which was then coated on composite substrates (1 cm×1 cm) as air cathodes [13]. Celgard 2340 membrane (A 38 μm microporous trilayer membrane with one polythylene layer between two polypropylene layers) was used a separator to prevent physical contact between the cathode and anode. The electrocatalyst loading was about 1.0 mg·cm^{-2}. The polarization curve was measured at a scan rate of 10 mV s^{-1} [14,15]. The galvanostatic recharge/discharge cycling measurements were collected on a CT-2001A testing system at a current density of 10 mA cm^{-2}. For comparison, the mixture slurry of RuO_2 and 20 wt% Pt/C with a mass ratio of 1:1 was dropwise added onto above-mentioned composite substrates with the area of 1 cm^{-2} to ensure a loading amount of 1 mg cm^{-2} as the air cathode. It was also used to assemble the Zn-air battery and performed the practical application at the same conditions.

The power density (mW cm^{-2}) and specific capacity (mAh g^{-1}) of zinc-air batteries with Pt/C + IrO_2 and Co_{SA}-RuO_2-NUCN based air cathode were determined by using following Equations 8 and 9.

$$Power\ density\ (mW\ cm^{-2}) = Voltage\ \times Current\ density \quad (8)$$

$$Specific\ capacity\ (mAh\ g^{-1}) = \frac{Current\ \times Service\ hours}{Weight\ of\ consumed\ Zn} \quad (9)$$

1.6 Computational methods

All calculations were conducted by Vienna abinitio simulation packages (VASP) within electronic wave function, which were expanded using the projector augmented wave method with an energy

cutoff of 400 eV to represent the basic set. The general gradient approximation (GGA) with Predew-Burker-Ernzerhof (PBE) was used to describe the exchange-correlation function. The wave function was optimized using an accuracy of 10-6 eV. The k point mesh of 2×2×1 was selected to treat the integration over the Brillouin zone for geometry optimization. 15 Å of vacuum separated slab in Z direction to avoid interaction between neighboring slabs.

2. Results and discussion

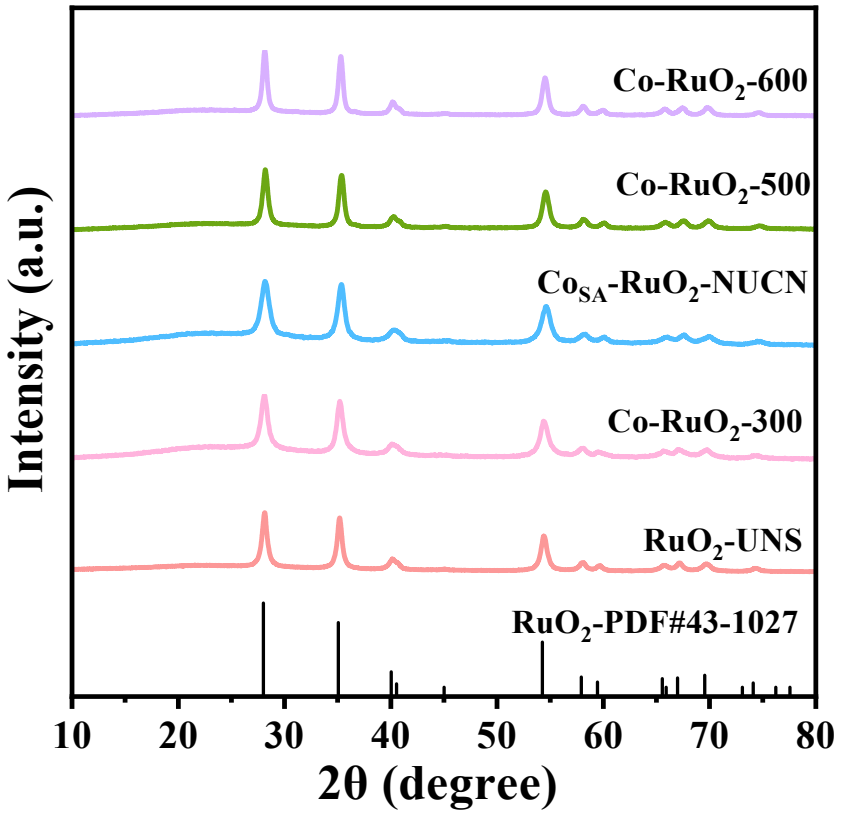

Fig. S1. XRD patterns of RuO_2-UNS, Co-RuO_2-300, Co_{SA}-RuO_2-NUCN, Co-RuO_2-500 and Co-RuO_2-600.

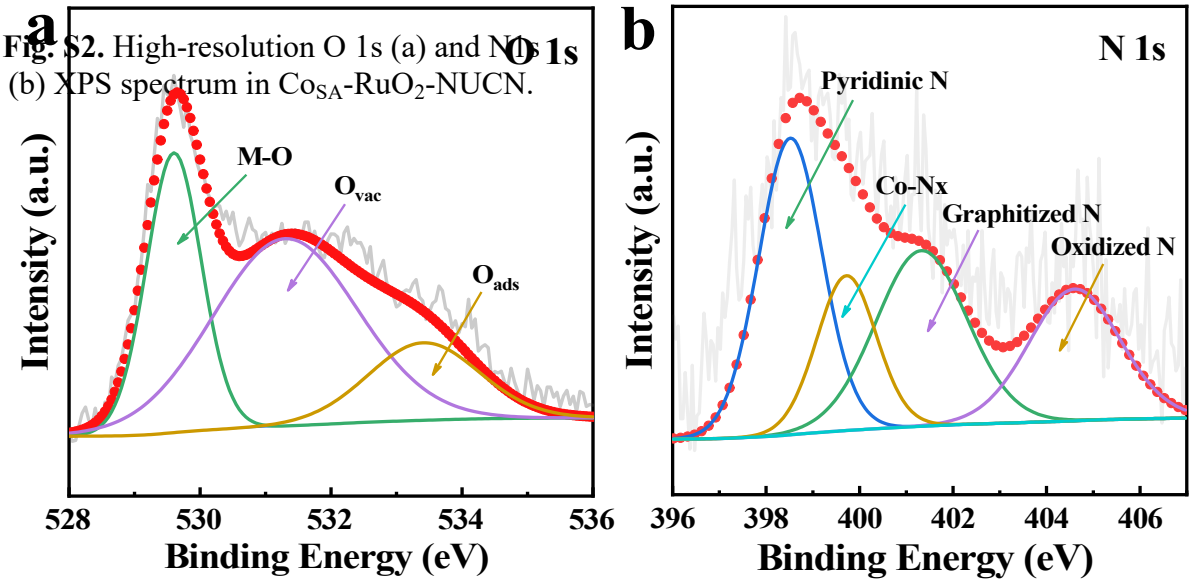

Fig. S2. High-resolution O 1s (a) and N 1s (b) XPS spectrum in Co_{SA}-RuO_2-NUCN.

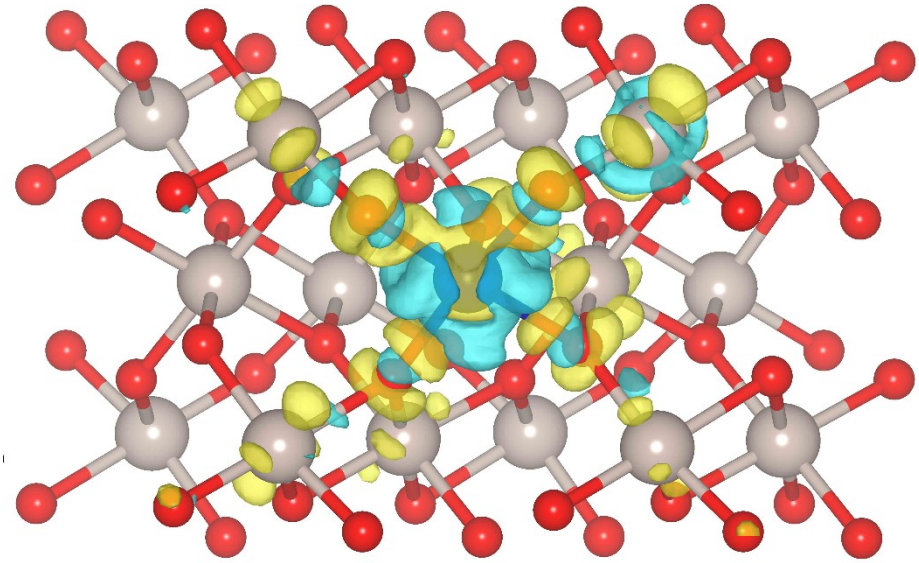

Fig. S3. Charge density difference diagrams (blue area for charge depletion and yellow area for charge accumulation). (Red-O atom, Gray-Ru atom, Purple-Co atom）

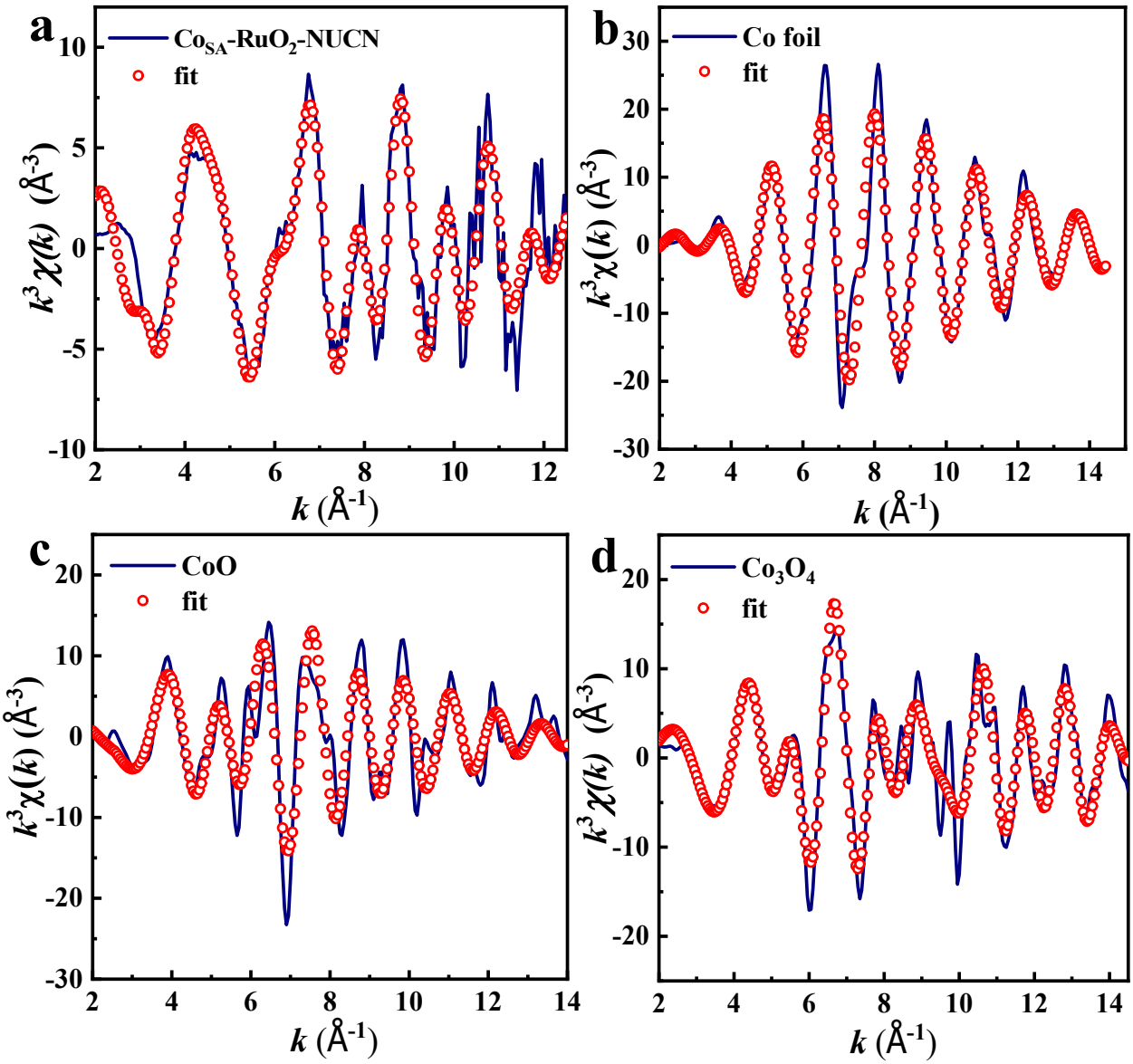

Fig. S4. Typical EXAFS fitting curves of Co for Co_{SA}-RuO_2-NUCN (a), Co foil (b), CoO (c) and Co_3O_4 (d) at K space.

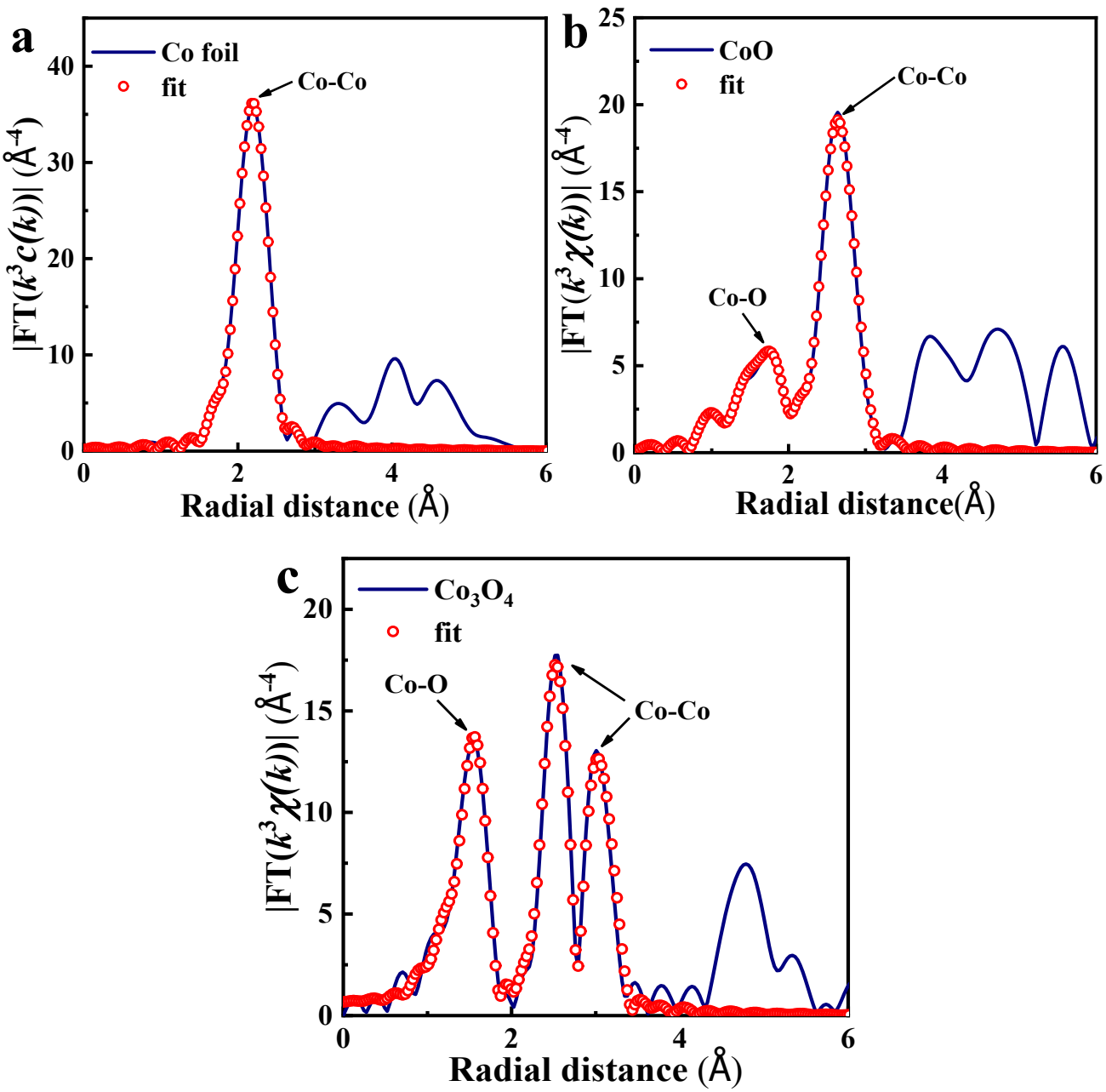

Fig. S5. The corresponding EXAFS fitting curve of Co foil (a), CoO (b) and Co_3O_4 (c) at R space.

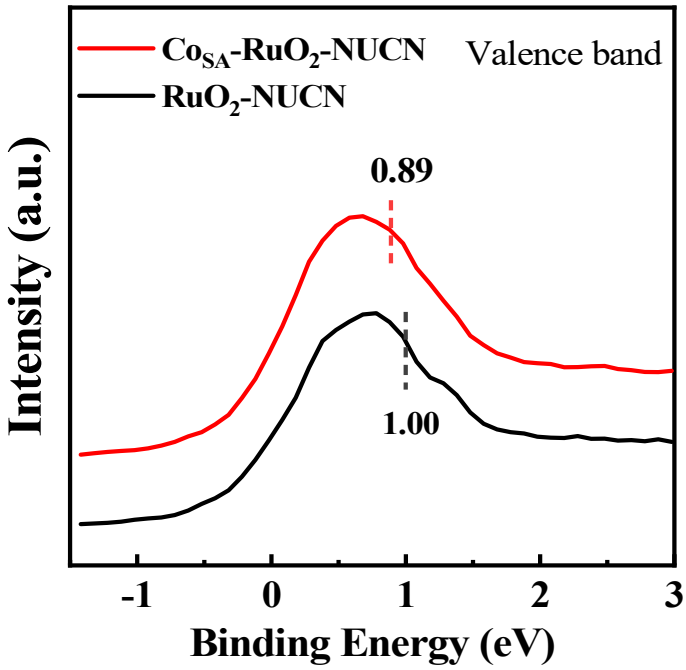

Fig. S6. The XPS valence band spectra and calculated d-band centers in the energy region between -1 and 3.

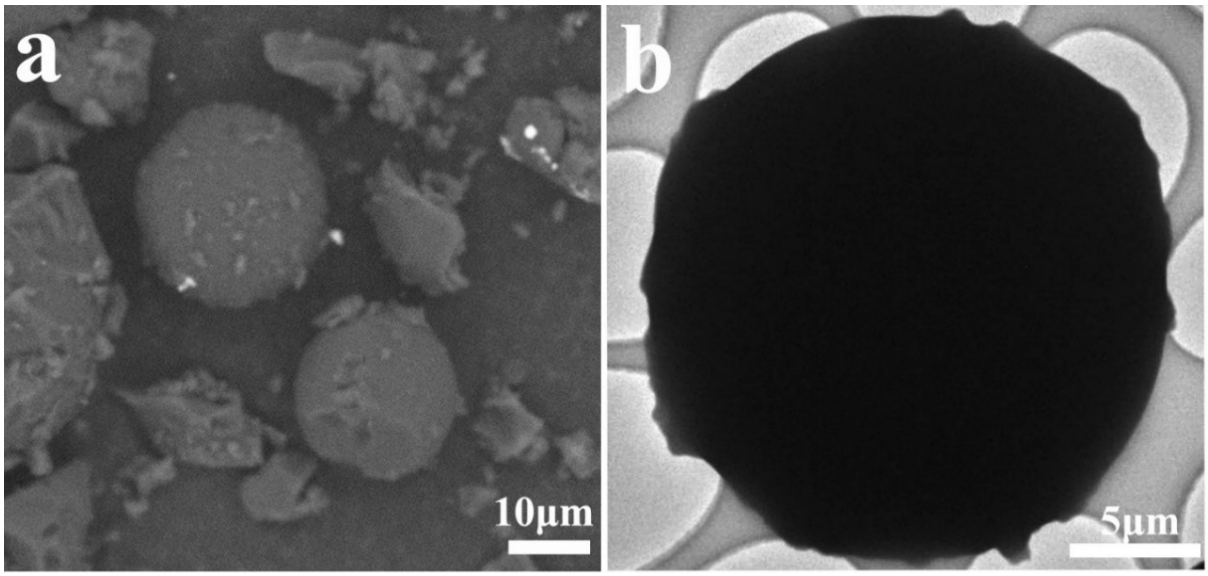

Fig. S7. Structural analyses of catalyst. SEM image of precursor (a) and TEM image of precursor (b).

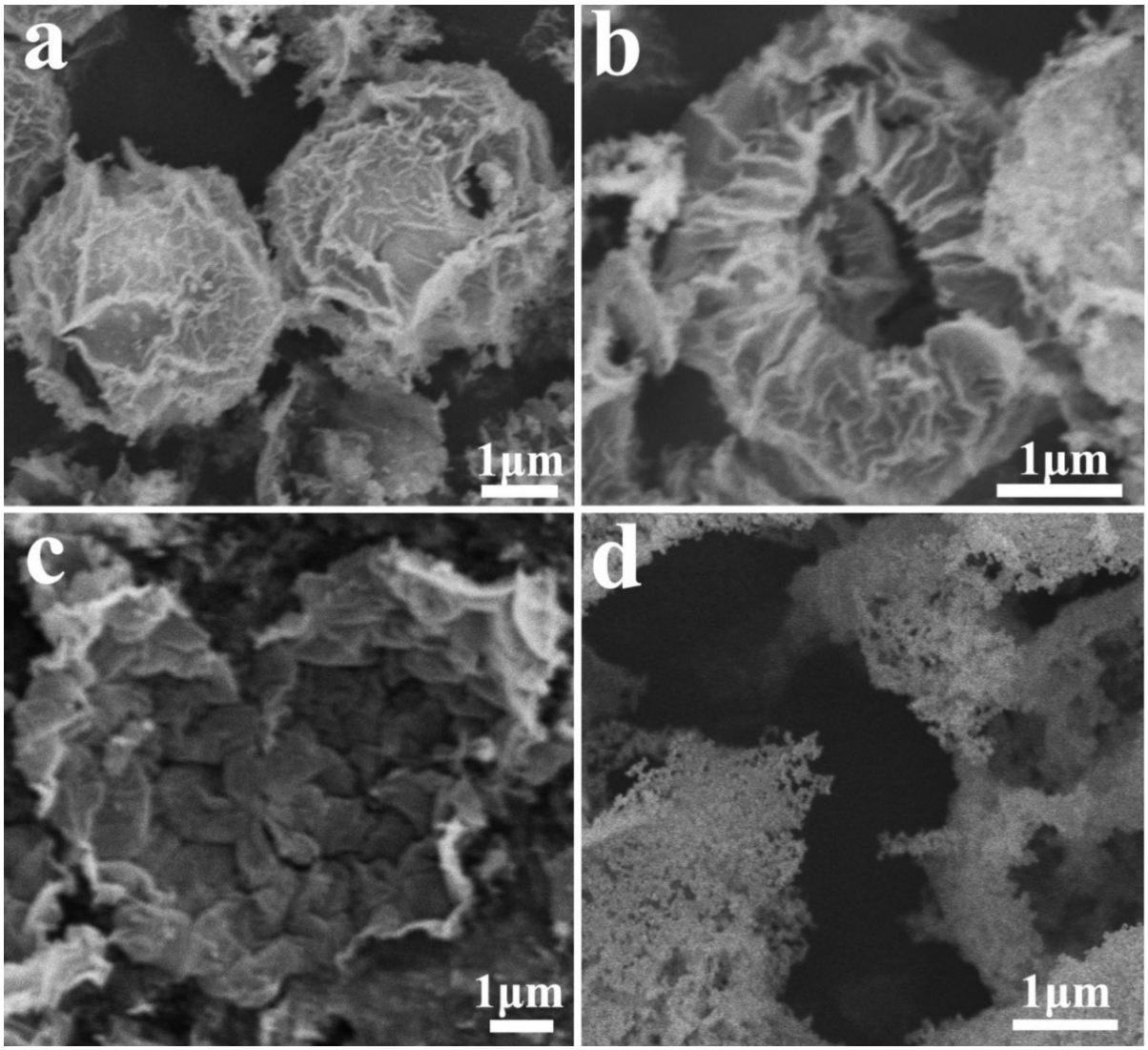

Fig. S8. Scanning electron microscopy (SEM) of Co_{SA}-RuO_2-NUCN with different oxidation time of 2h (a), 4h (b), 6h (c) and 8h (d).

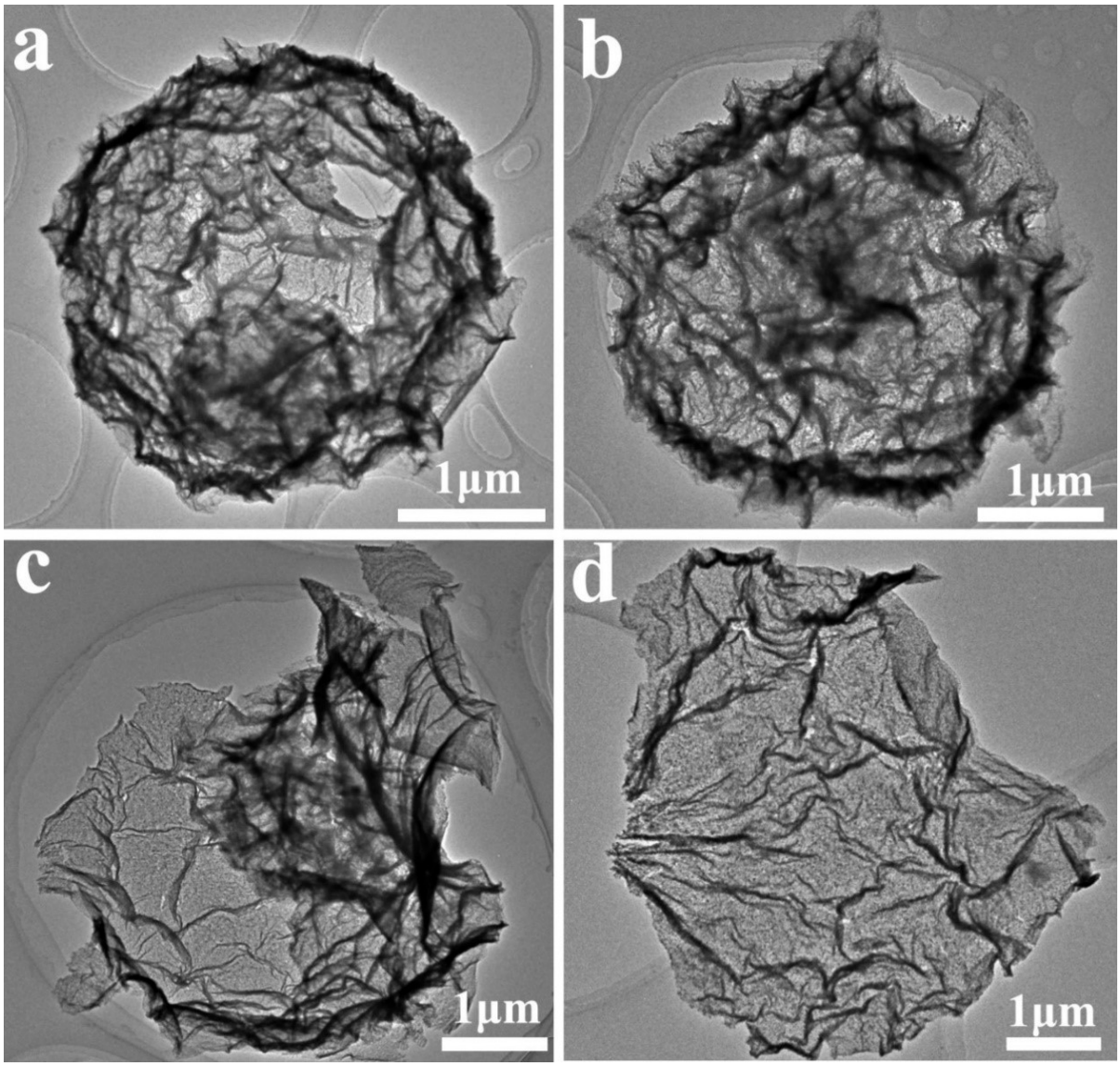

Fig. S9. Transmission electron microscope (TEM) of Co_{SA}-RuO_2-NUCN with different oxidation time of 2h (a), 4h (b), 6h (c) and 8h (d).

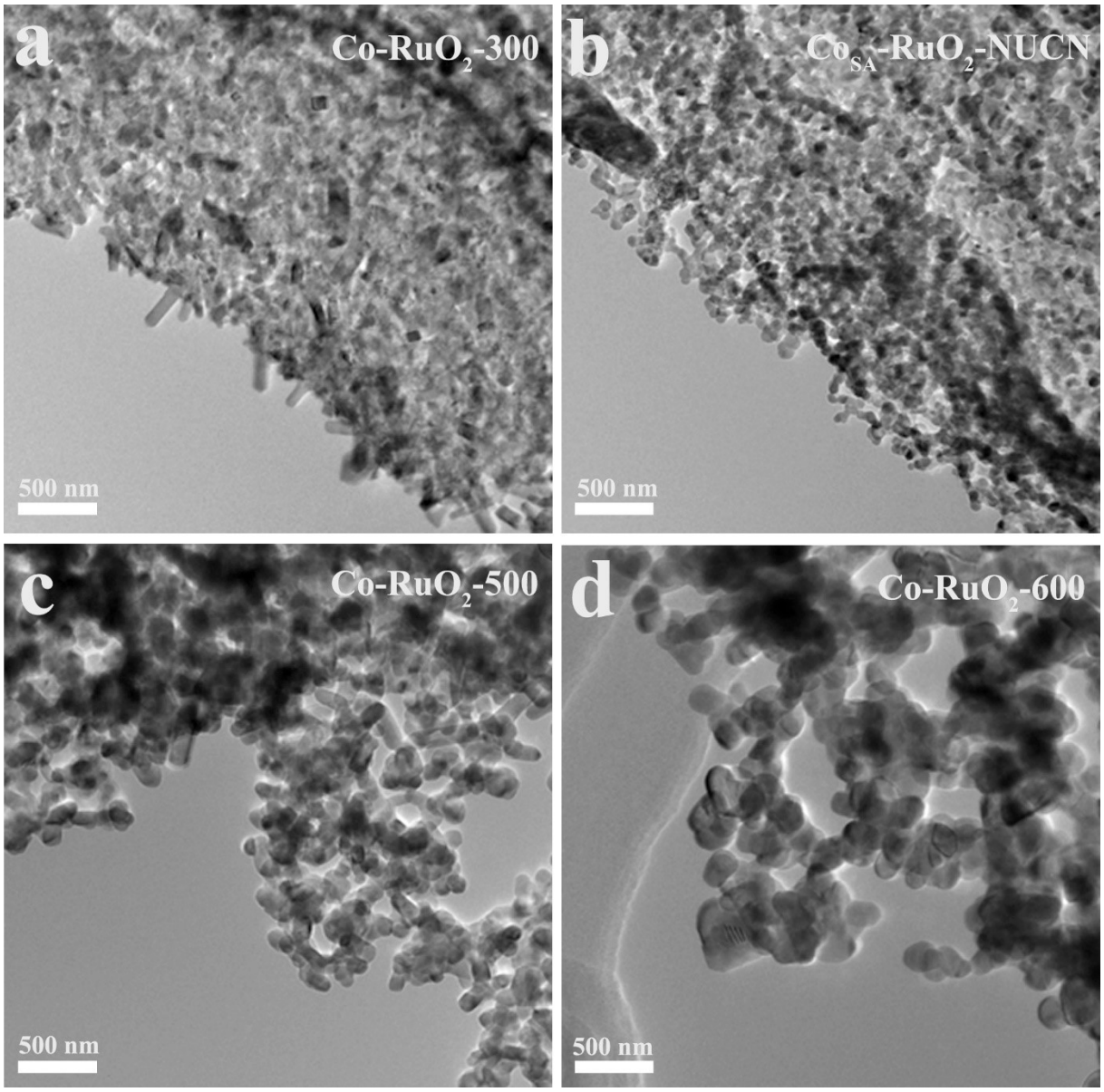

Fig. S10. Transmission electron microscope (TEM) of Co_{SA}-RuO_2-NUCN with different oxidation temperature of 300℃ (a), 400℃ (b), 500℃ (c) and 600℃ (d).

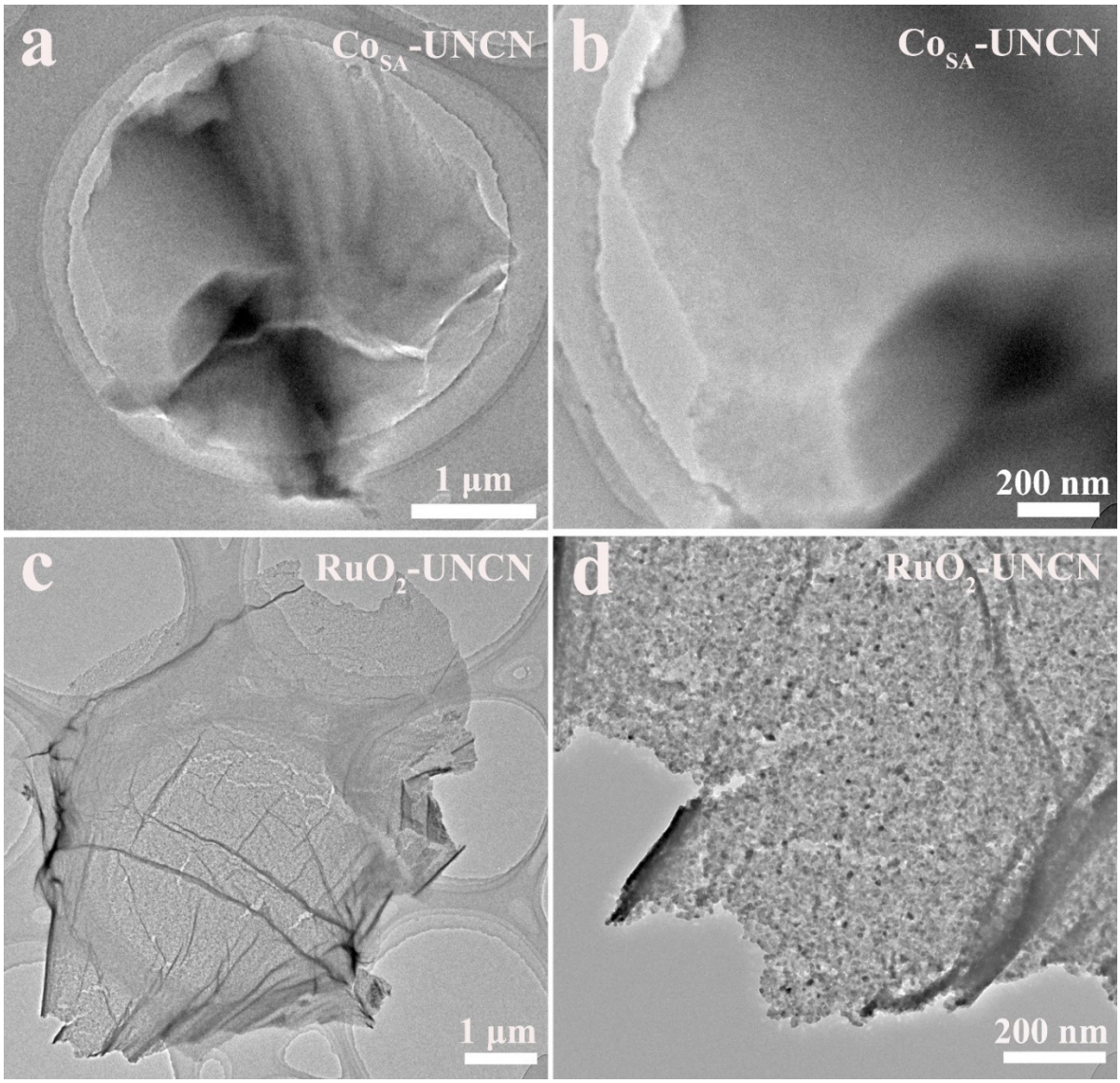

Fig. S11. Transmission electron microscope (TEM) of Co_{SA}-NUCN (a, b) and RuO_2-NUCN (c, d).

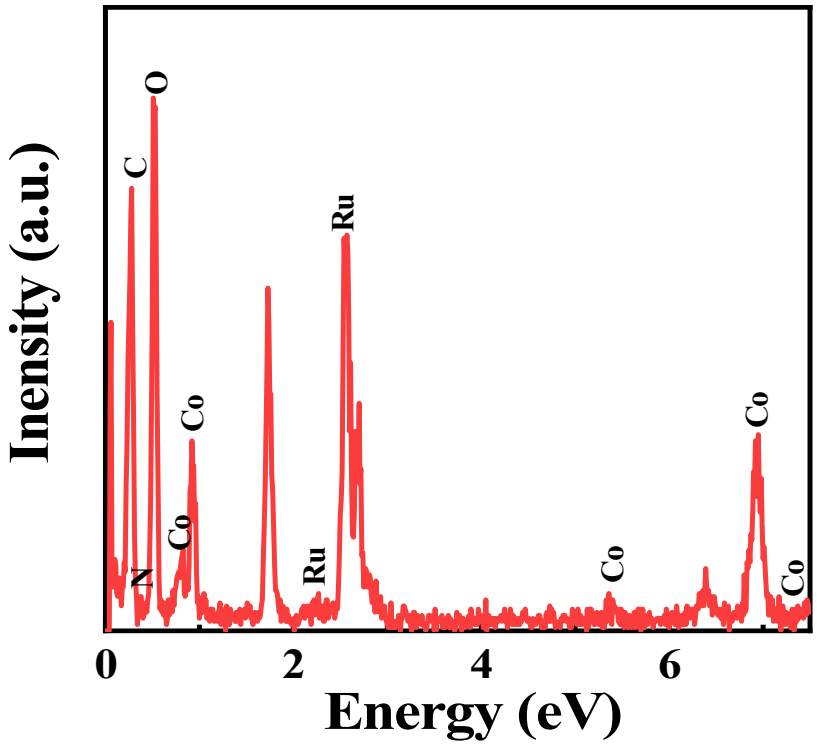

Fig. S12. EDS curve for elemental determination in Co_{SA}-RuO_2-NUCN.

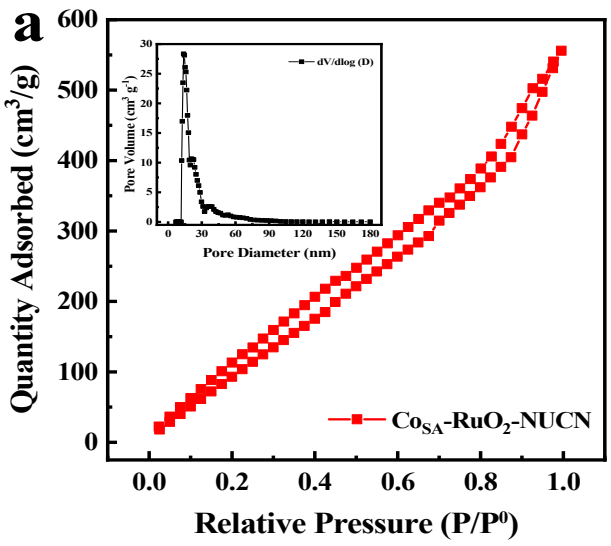

Fig. S13. N_2 adsorption-desorption isotherms of Co_{SA}-RuO_2-NUCN (a) and RuO_2-NUCN (b).

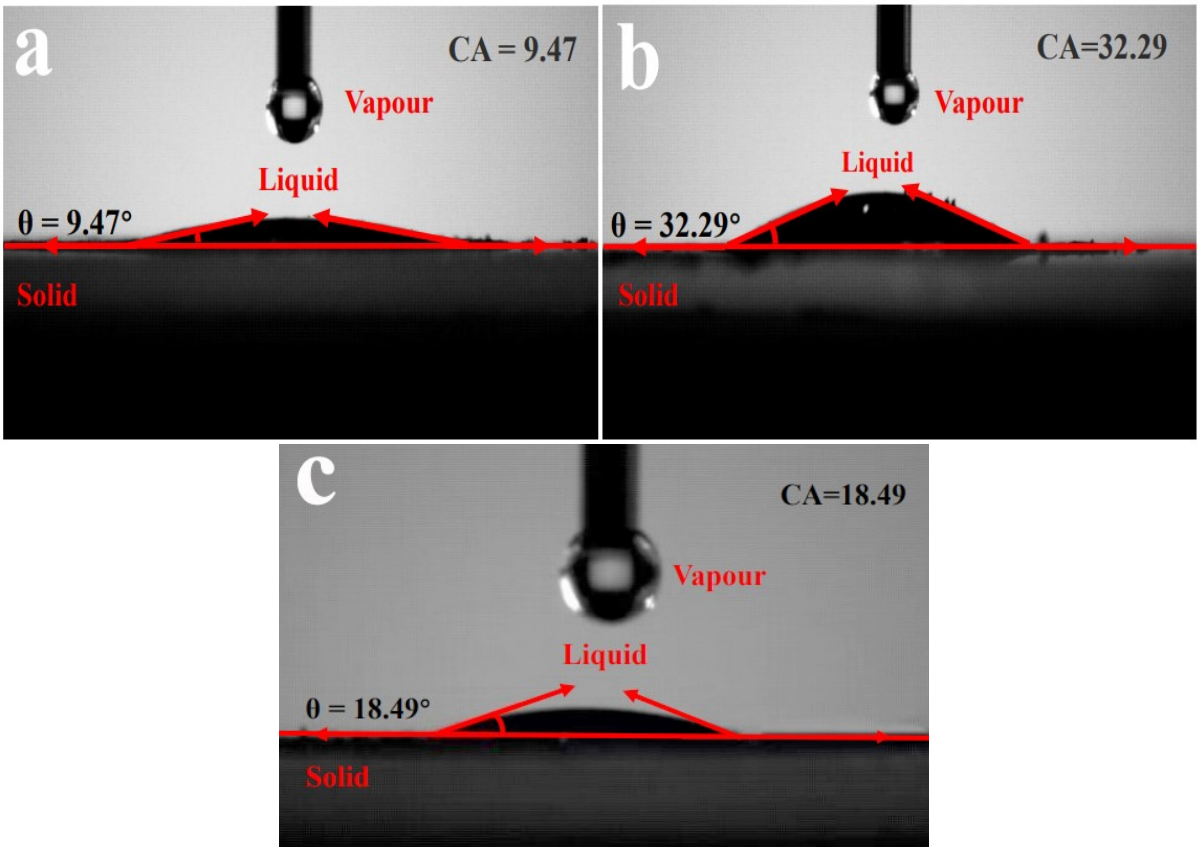

Fig. S14. Contact angles of Co_{SA}-RuO_2-NUCN (a); RuO_2-NUCN (b) and Co_{SA}- NUCN (c).

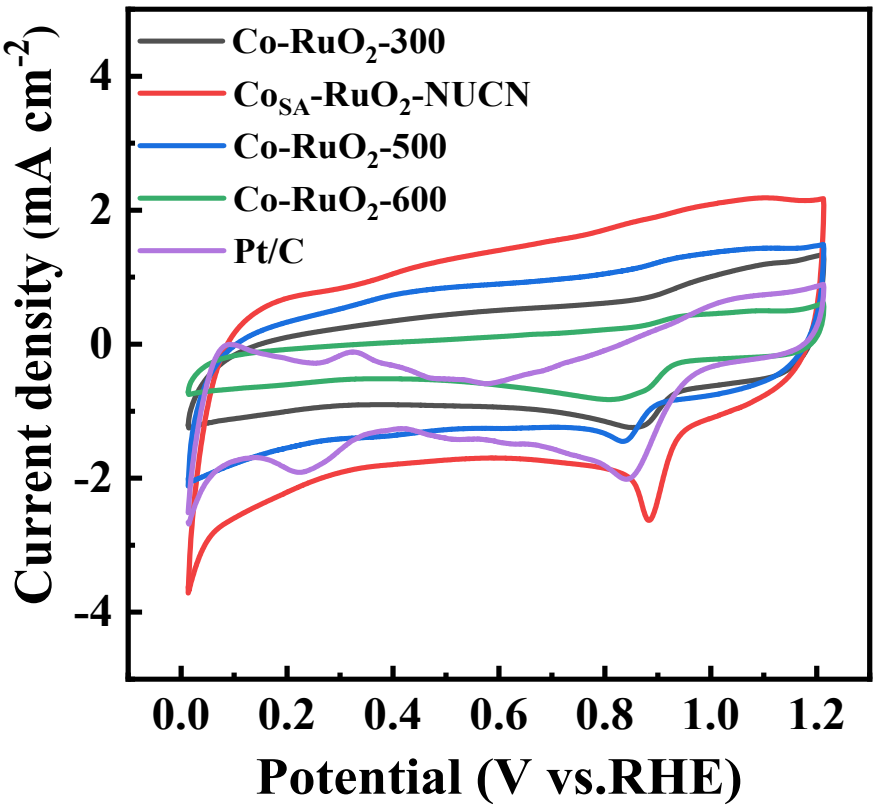

Fig. S15. CV curves for Co-RuO_2-300, Co_{SA}-RuO_2-NUCN, Co-RuO_2-500, Co-RuO_2-600 and Pt/C in 0.1 M KOH electrolyte at 10 mV s^{-1}.

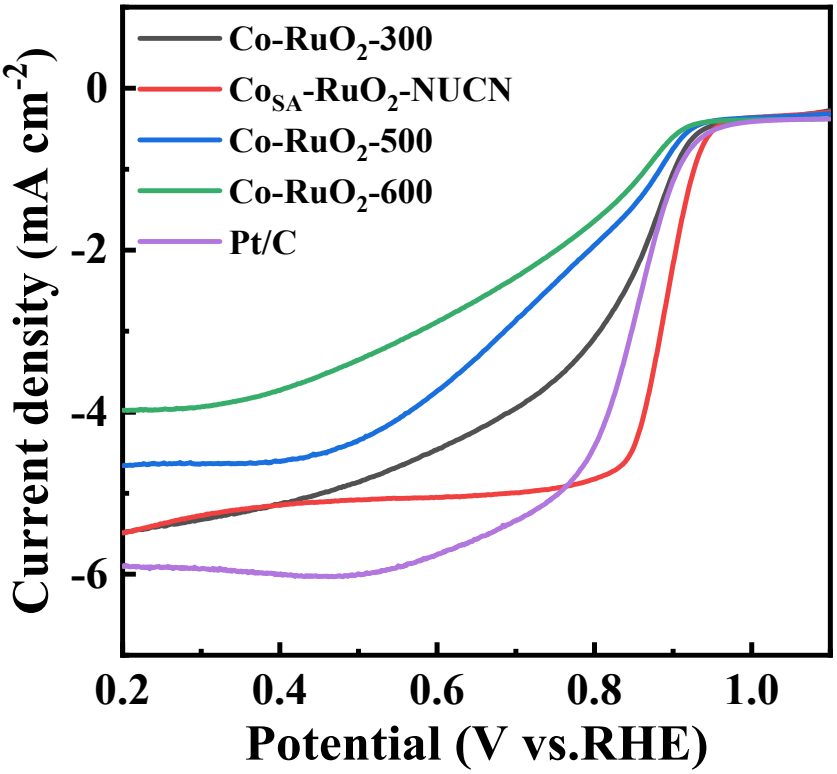

Fig. S16. LSV curves of Co-RuO_2-300, Co_{SA}-RuO_2-NUCN, Co-RuO_2-500, Co-RuO_2-600 and Pt/C in an O_2-saturated 0.1 M KOH solution at a scan rate of 5 mV s^{-1}.

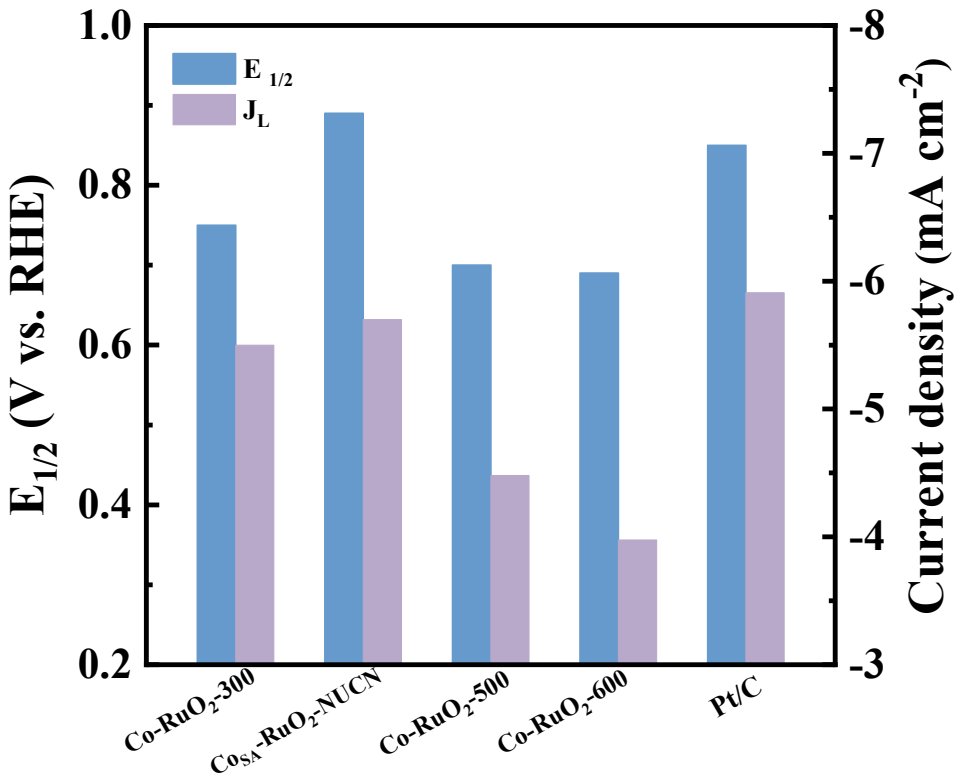

Fig. S17. Kinetic current densities and half wave potentials of Co-RuO_2-300, Co_{SA}-RuO_2-NUCN, Co-RuO_2-500, Co-RuO_2-600 and Pt/C.

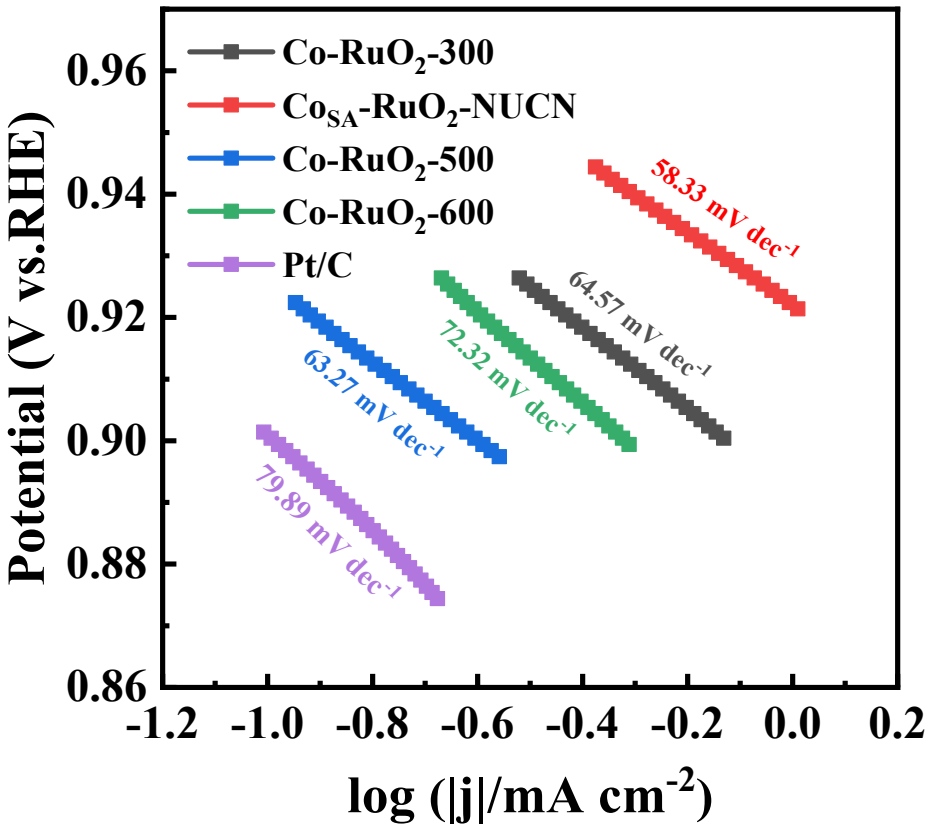

Fig. S18. Tafel plots of Tafel plots of the Co-RuO_2-300, Co_{SA}-RuO_2-NUCN, Co-RuO_2-500, Co-RuO_2-600 and Pt/C in 0.1 M KOH solution.

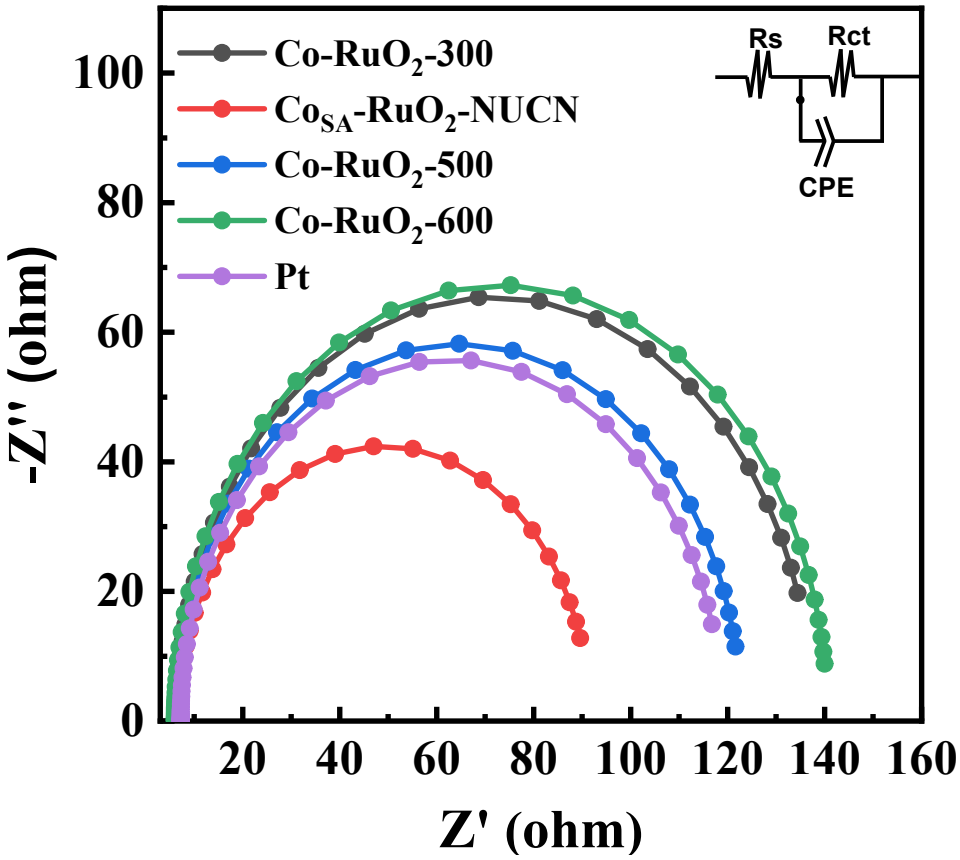

Fig. S19. Nyquist curves of Co-RuO_2-300, Co_{SA}-RuO_2-NUCN, Co-RuO_2-500, Co-RuO_2-600 and Pt/C in an O_2-saturated 0.1 M KOH solution at an amplitude of 5 mV with a rotation rate of 1600 rpm for ORR.

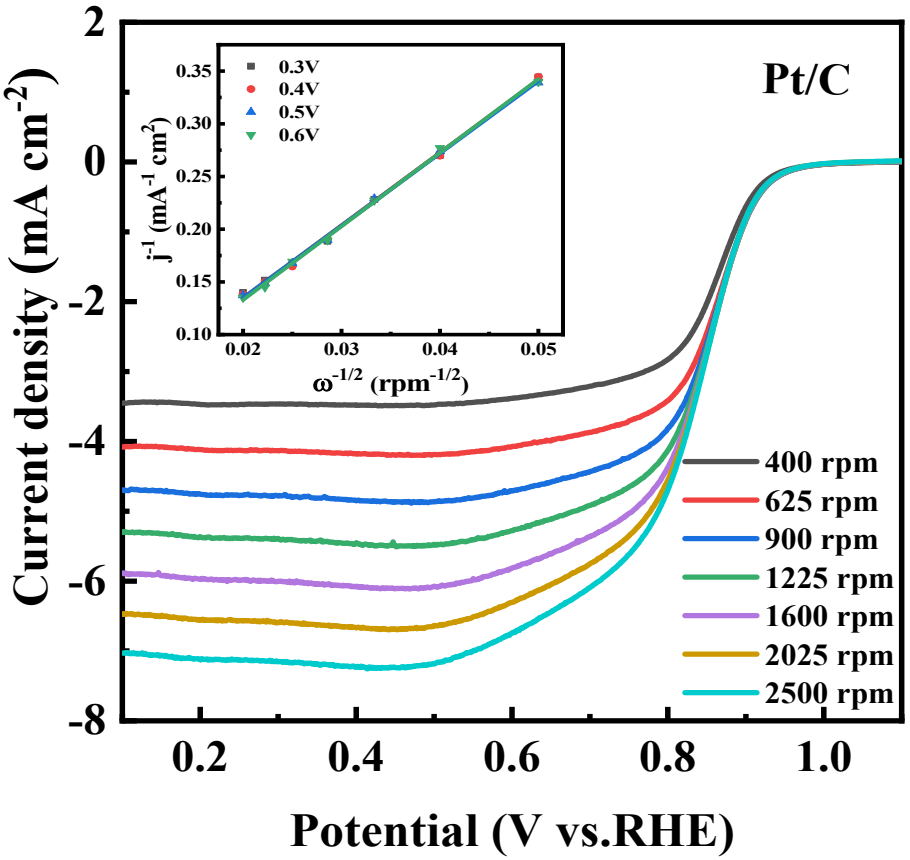

Fig. S20. LSV curves and calculated K-L plots (inset) of Pt/C at different potentials in an O_2-saturated 0.1 M KOH at different RDE rotation rates (5 mV s^{-1}).

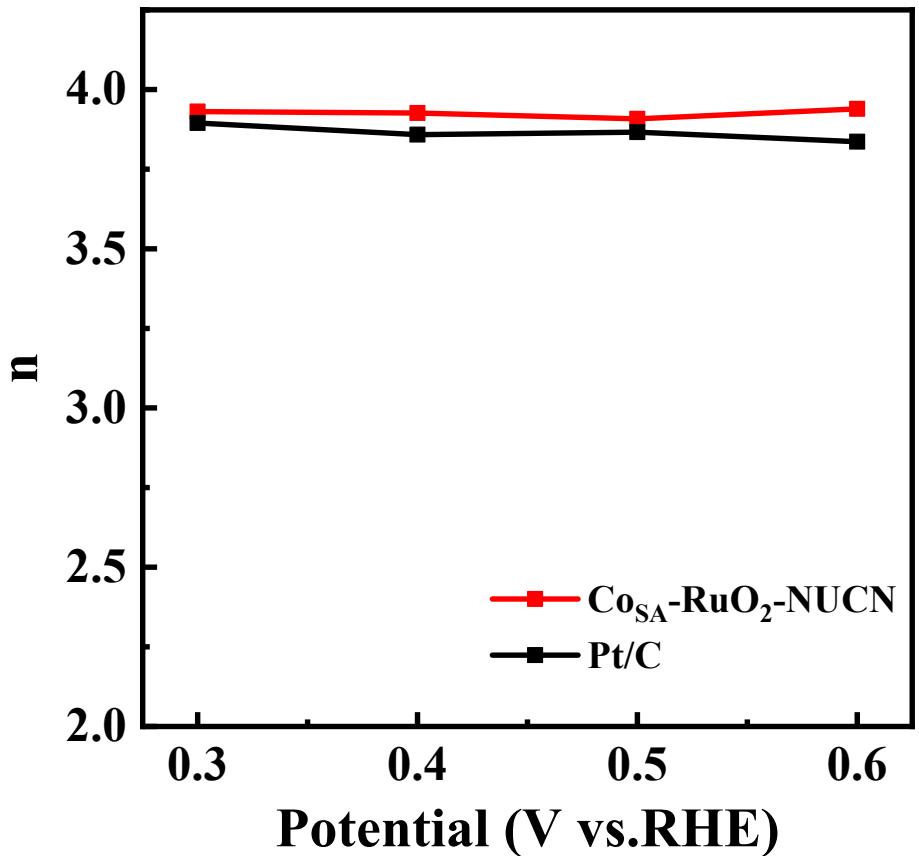

Fig. S21. Electron-transfer number (n) derived from K-L plots at different potentials.

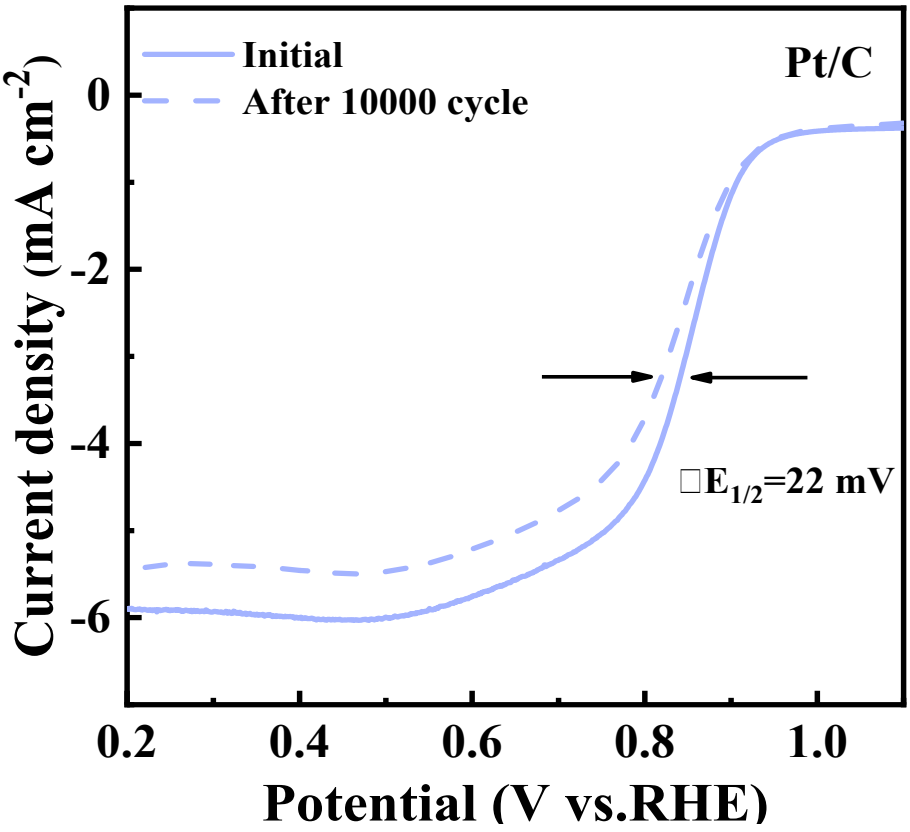

Fig. S22. ORR polarization curves of Pt/C before and after the continuous operation in the O_2-saturated 0.1 M KOH at 1600 rpm.

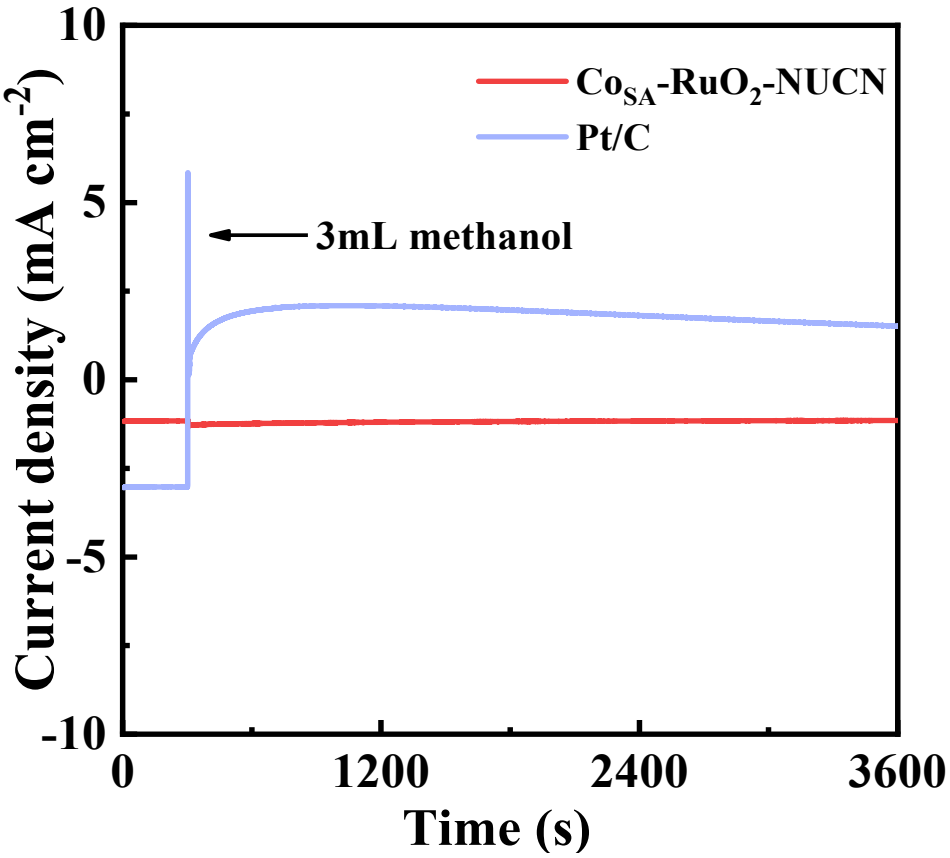

Fig. S23. Chronoamperometric (i-t) responses of Co_{SA}-RuO_2-NUCN and Pt/C after the addition of 1 M methanol in an O_2-saturated 0.1 M KOH at 1600 rpm.

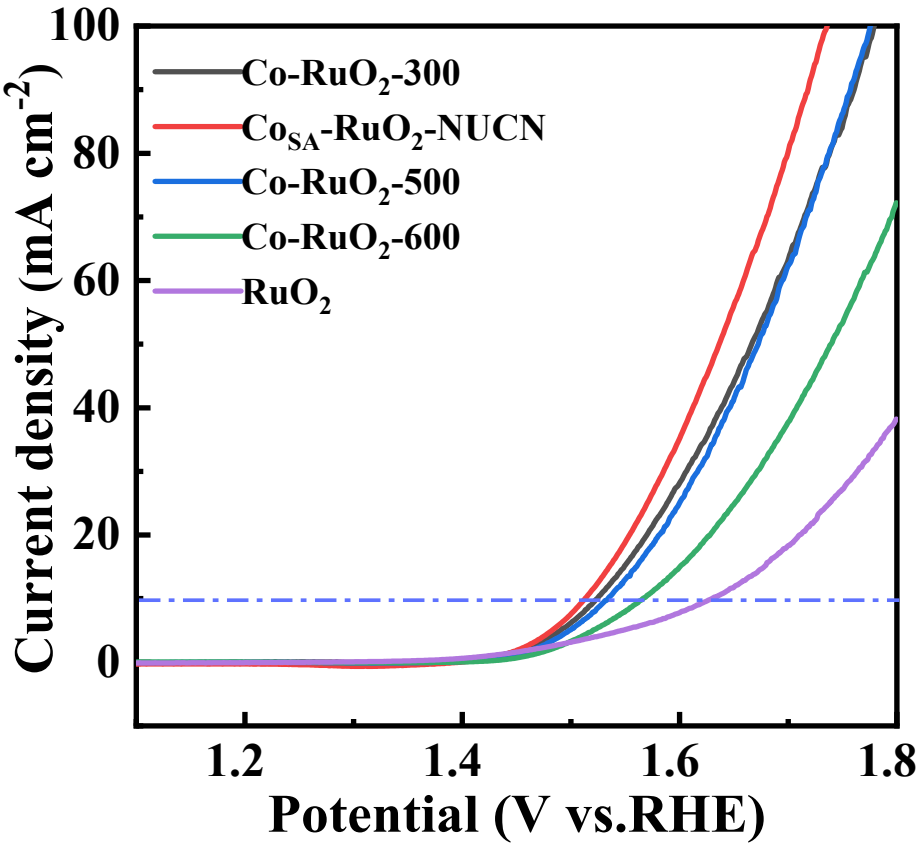

Fig. S24. LSV curves of Co-RuO_2-300, Co_{SA}-RuO_2-NUCN, Co-RuO_2-500, Co-RuO_2-600 and RuO_2 in an O_2-saturated 0.1 M KOH solution at a scan rate of 2 mV s^{-1} and 1600 rpm.

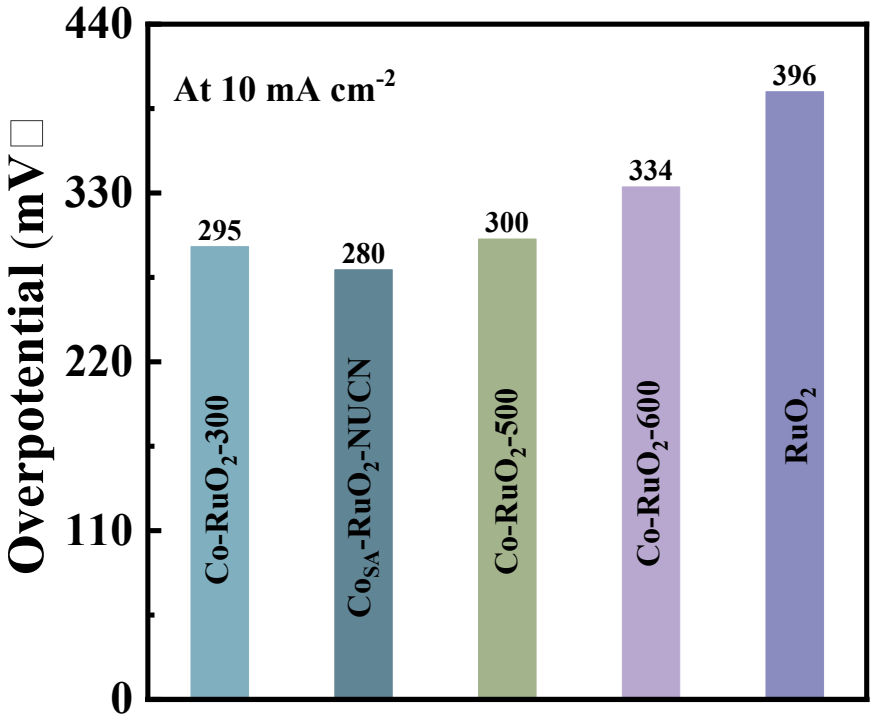

Fig. S25. The corresponding overpotential of Co-RuO_2-300, Co_{SA}-RuO_2-NUCN, Co-RuO_2-500, Co-RuO_2-600 and RuO_2 in 0.1 M KOH solution.

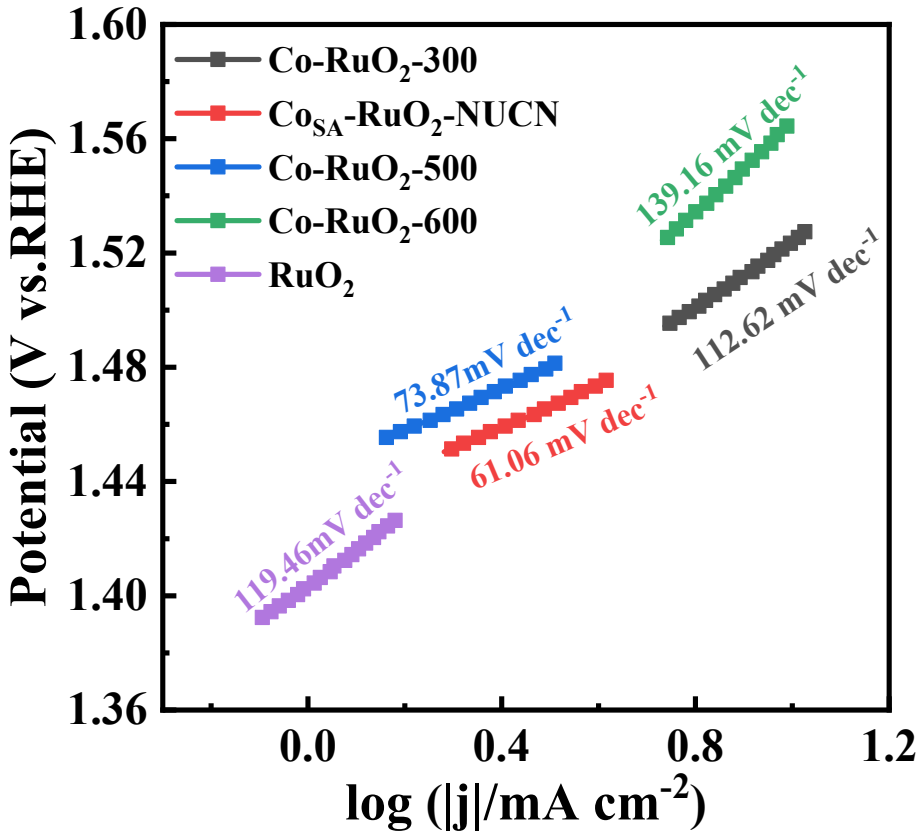

Fig. S26. Tafel plots of Co-RuO_2-300, Co_{SA}-RuO_2-NUCN, Co-RuO_2-500, Co-RuO_2-600 and RuO_2 in 0.1 M KOH solution.

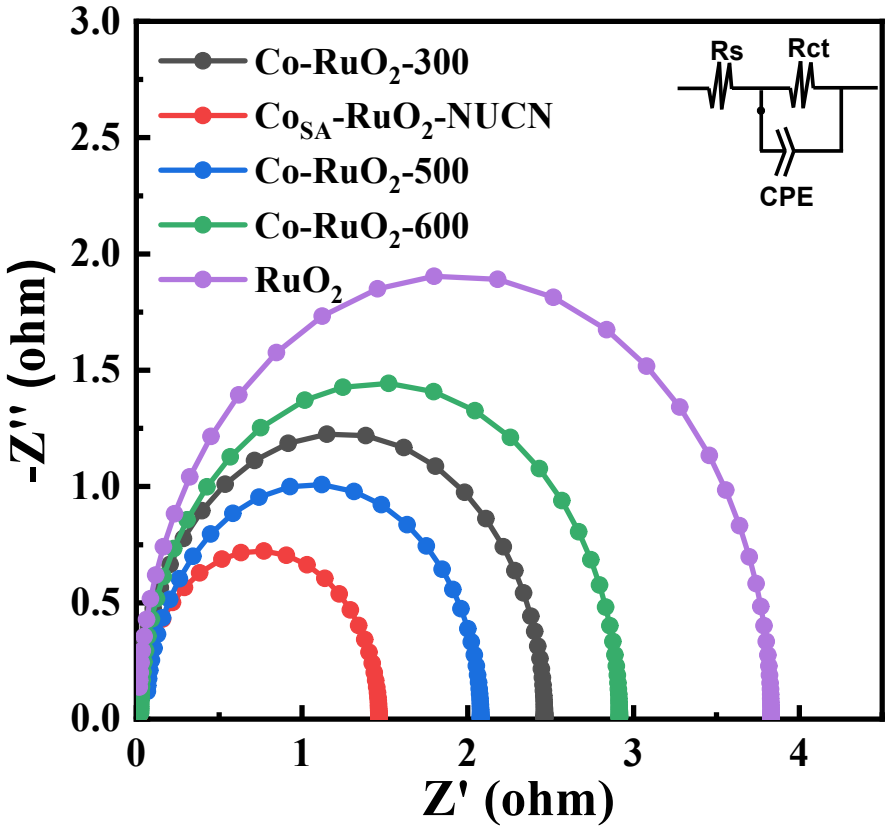

Fig. S27. Nyquist curves of Co-RuO_2-300, Co_{SA}-RuO_2-NUCN, Co-RuO_2-500, Co-RuO_2-600 and RuO_2 in an O_2-saturated 0.1 M KOH solution at an amplitude of 5 mV with a rotation rate of 1600 rpm for OER.

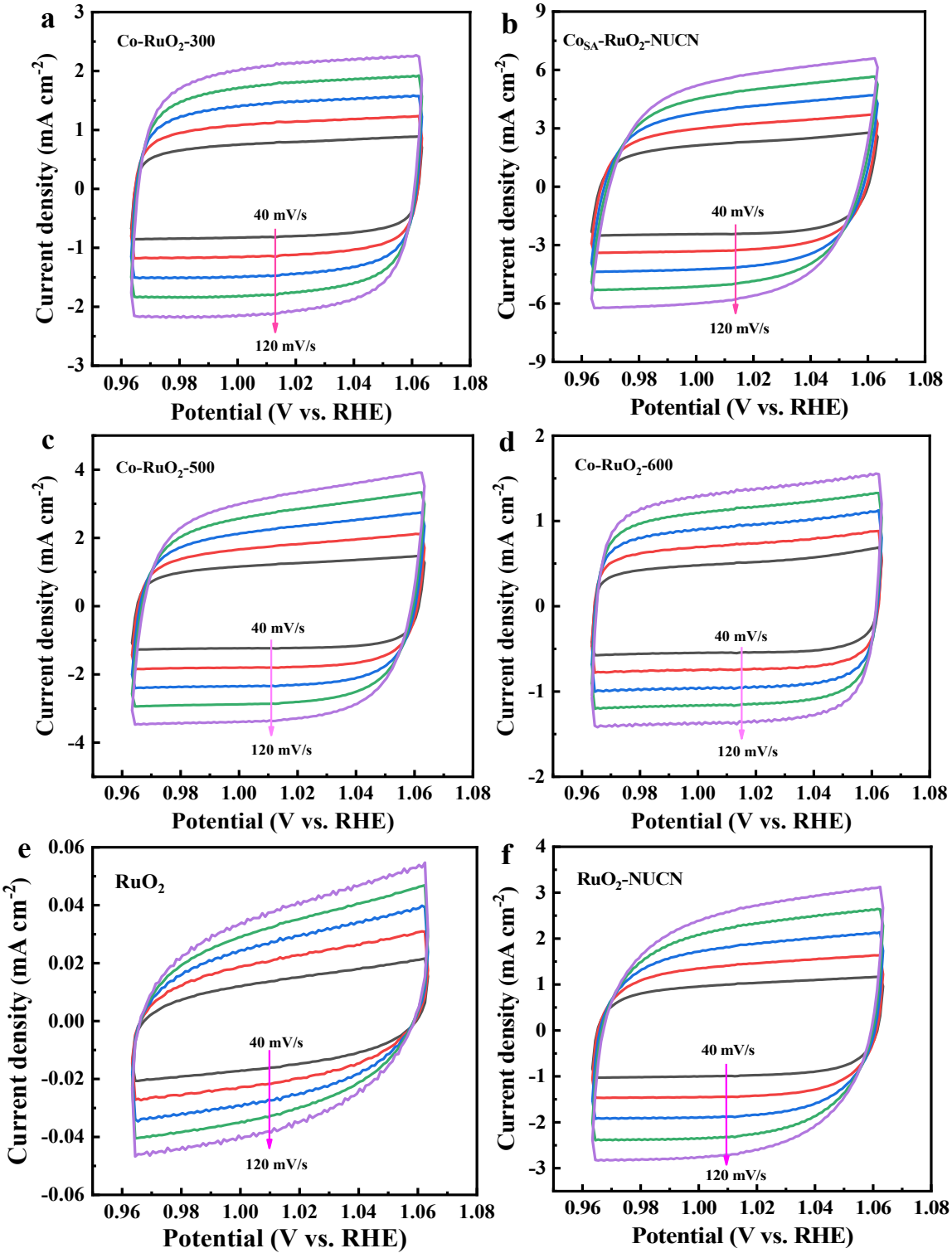
a
Co-RuO2-300
Current density (mA cm-2)
40 mV/s
120 mV/s
Potential (V vs. RHE)
b
CoSA-RuO2-NUCN
Current density (mA cm-2)
40 mV/s
120 mV/s
Potential (V vs. RHE)
c
Co-RuO2-500
Current density (mA cm-2)
40 mV/s
120 mV/s
Potential (V vs. RHE)
d
Co-RuO2-600
Current density (mA cm-2)
40 mV/s
120 mV/s
Potential (V vs. RHE)
e
RuO2
Current density (mA cm-2)
40 mV/s
120 mV/s
Potential (V vs. RHE)
f
RuO2-NUCN
Current density (mA cm-2)
40 mV/s
120 mV/s
Potential (V vs. RHE)

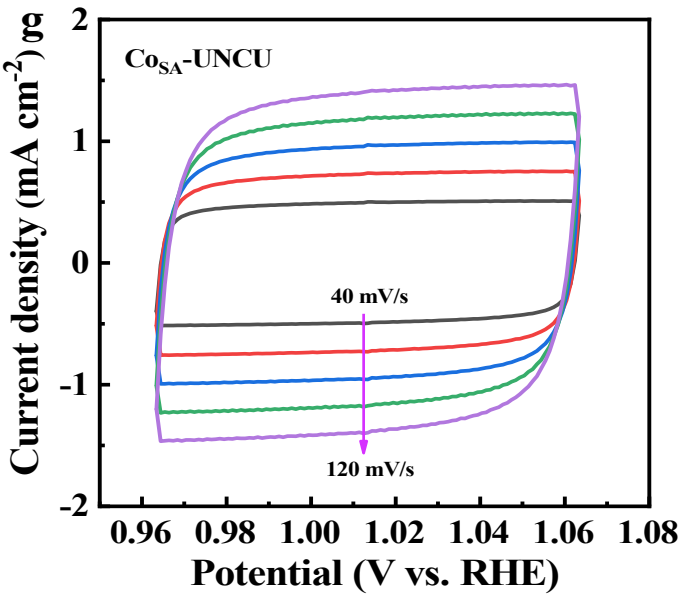

Fig. S28. CV curves of Co-RuO_2-300 (a), Co_{SA}-RuO_2-NUCN (b), Co-RuO_2-500 (c), Co-RuO_2-600 (d), RuO_2 (e), RuO_2-NUCN (f) and Co_{SA}-NUCN (g) in 0.1 M KOH electrolyte at different scan rates.

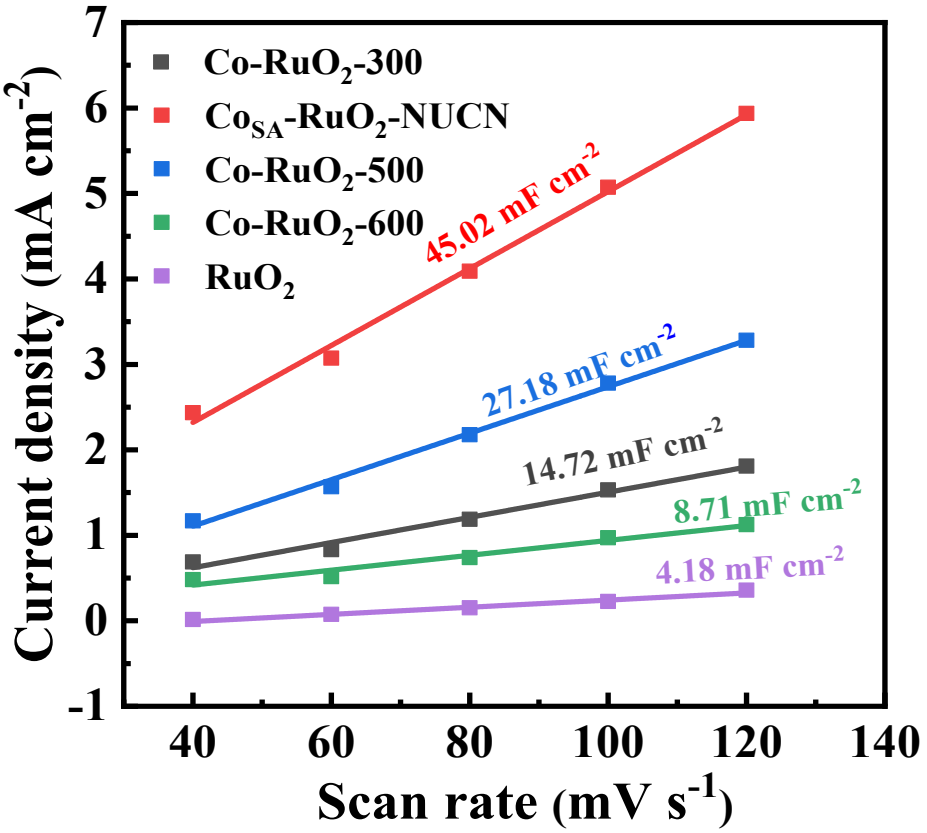

Fig. S29. Linear plots of scan rates vs. current density for Co-RuO_2-300, Co_{SA}-RuO_2-NUCN, Co-RuO_2-500, Co-RuO_2-600 and RuO_2 in 0.1 M KOH electrolyte.

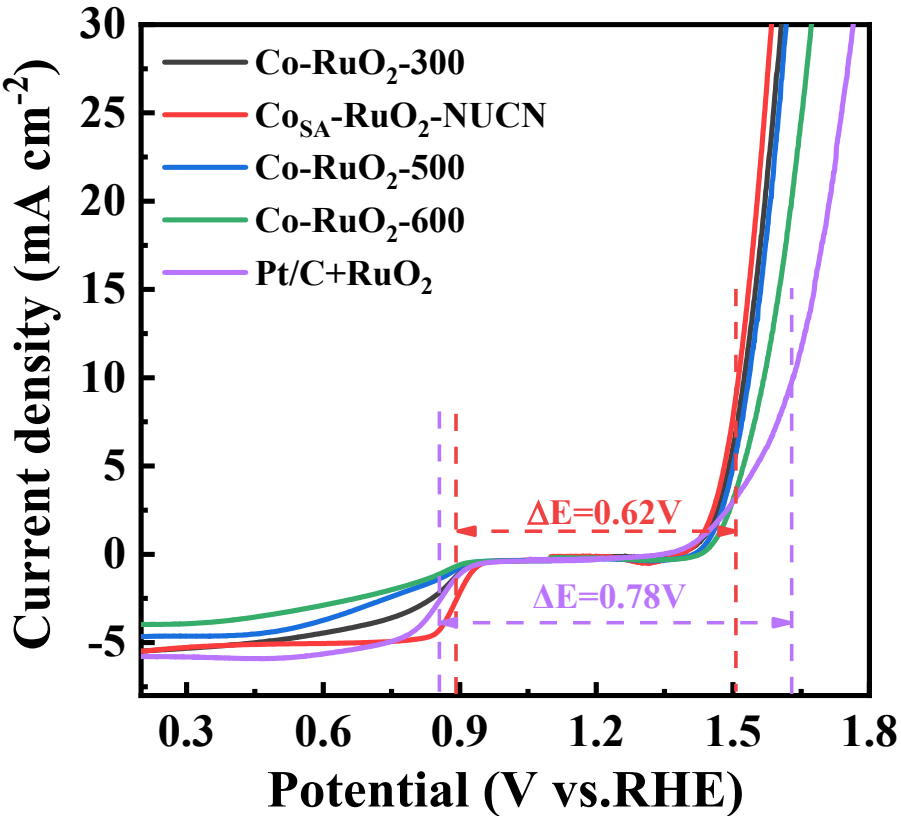

Fig. S30. ORR/OER polarization curves of Co-RuO_2-300, Co_{SA}-RuO_2-NUCN, Co-RuO_2-500, Co-RuO_2-600 and Pt/C+RuO_2.

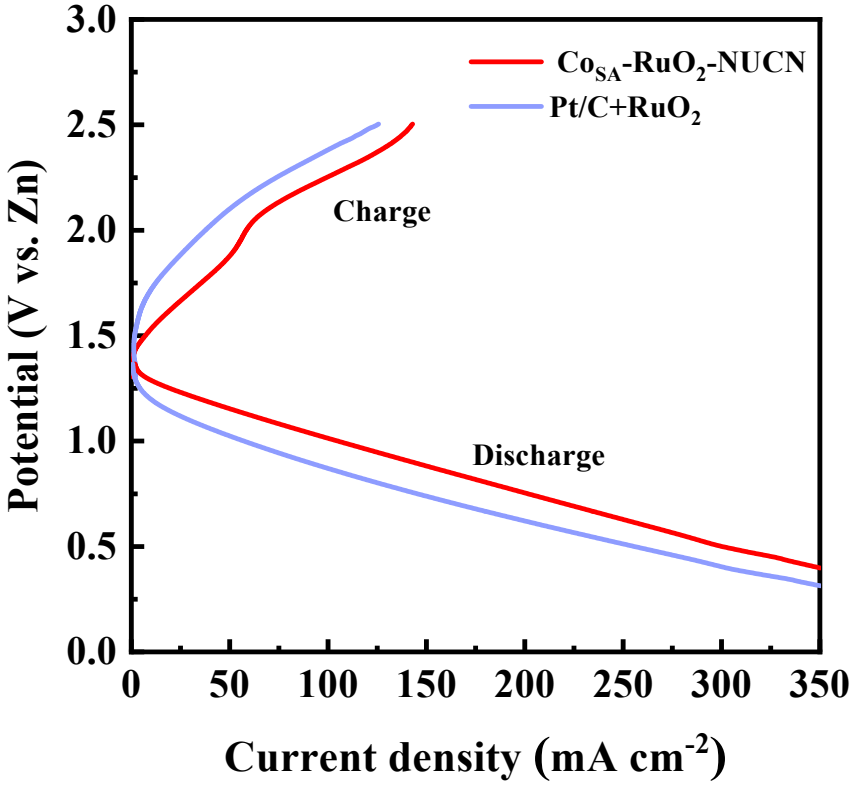

Fig. S31. Discharge and charge polarization curves of ZAB cells with Co_{SA}-RuO_2-NUCN and Pt/C+RuO_2 mixture cathodes.

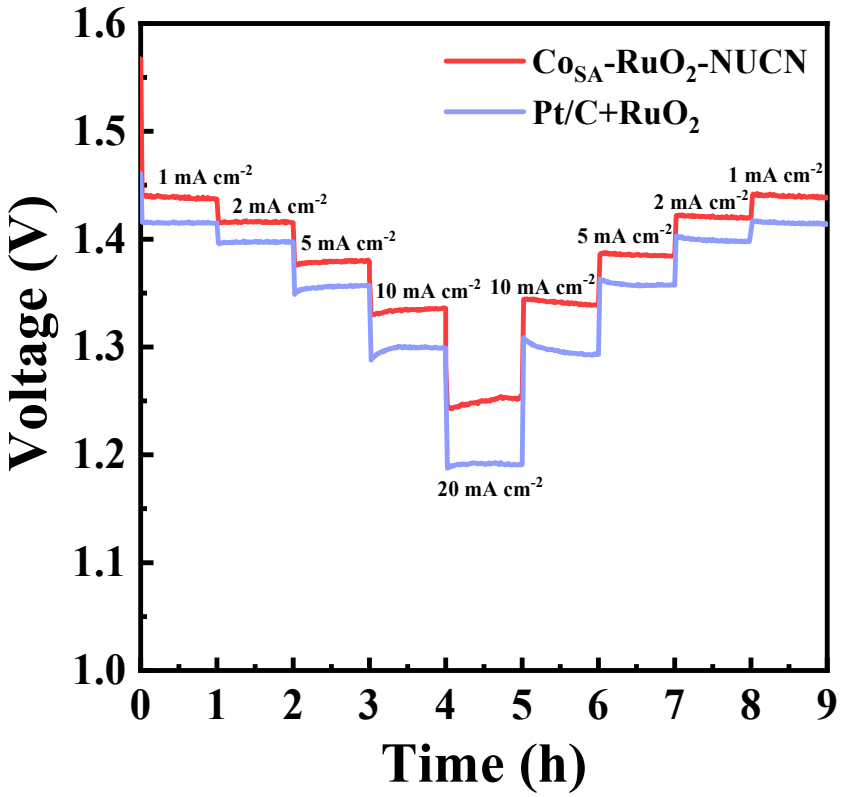

Fig. S32. Discharge curves at various discharge current densities of Co_{SA}-RuO_2-NUCN and Pt/C+RuO_2 mixture cathodes.

Table S1. EXAFS fitting parameters at the Co *K*-edge for various samples（S_0^2=0.743）

Sample	Shell	CN[a]	R(Å)[b]	σ²(Å²)[c]	ΔE₀(eV)[d]	R factor
Co foil	Co-Co	12*	2.494±0.001	0.0064±0.0002	7.9±0.3	0.0017
CoO	Co-O	6.0±0.3	2.108±0.016	0.0103±0.0021	-1.1±6.6	0.0051
	Co-Co	11.7±0.5	3.007±0.008	0.0087±0.0009	1.7±1.4	
Co_3O_4	Co-O	5.9±0.5	1.916±0.007	0.0033±0.0007	3.9±1.2	0.0072
	Co-Co	5.9±0.5	2.855±0.005	0.0048±0.0004	2.0±0.8	
	Co-Co	7.4±0.7	3.357±0.006			
Co_{SA}-RuO_2-NUCN	Co-O	6.2±0.8	1.903±0.010	0.0063±0.0013	-1.4±2.1	0.0105
	Co-O-Ru	3.1±0.8	3.344±0.017	0.0047±0.0018	6.6±2.6	

[a]*CN*, coordination number; [b]*R*, the distance to the neighboring atom; [c]σ^2, the Mean Square Relative Displacement (MSRD); [d]ΔE_0, inner potential correction; *R* factor indicates the goodness of the fit. $S0^2$ was fixed to 0.743, according to the experimental EXAFS fit of Co foil by fixing *CN* as the known crystallographic value. * This value was fixed during EXAFS fitting, based on the known structure of Co. Fitting range: $3.0 \le k$ (/Å) ≤ 14.1 and $1.0 \le R$ (Å) ≤ 3.0 (Co foil); $3.0 \le k$ (/Å) ≤ 12.0 and $1.0 \le R$ (Å) ≤ 4.0 (mxn-1-1). A reasonable range of EXAFS fitting parameters: $0.700 < S_0^2 < 1.000$; $CN > 0$; $\sigma^2 > 0$ Å^2; $|\Delta E_0| < 10$ eV; *R* factor < 0.02.

Table S2. Cobalt content of Co_{SA}-RuO_2-NUCN.

Samples	Co (mas.%) from ICP-OES
Co_{SA}-RuO_2-NUCN	0.46

Table S3. Comparison of the E gap values, OER overpotential and mass activity of Co_{SA}-RuO_2-NUCN with state-of-the-art bifunctional electrocatalysts.

Electrocatalysts	E_{gap} (V)	OER Overpotential (mV)	Mass activity ($A\ g^{-1}$)	Reference
Co_{SA}-RuO_2-NUCN	**0.62**	**280**	**66.67 ± 0.01**	**This work**
BrHT@CoNC	0.6	254	-	*J. Mater. Chem. A* **8**, 10865-10874 (2020)
Co@N-C/PCNF	0.67	289	4.76 ± 0.01	*Adv. Sci*. **8**, 2101438 (2021)
Co_2Cu_1-S	0.74	331	27.70 ± 0.01	*J. Mater. Chem. A* **9**, 18329-18337 (2021)
Co_3O_4 @Z67-N700@CeO_2	0.72	370	-	*J. Mater. Chem. A* **7**, 25853-25864 (2020)
Co/Co-N-C	0.76	410	21.78 ± 0.01	*J. Power Sources* **458**, 229339 (2021)
CoFe/SN-C	0.66	274	-	*Appl. Catal., B* **269**, 118771 (2020)
Co/MnO@NC	0.66	260	50.00 ± 0.01	*Energy Storage Mater.* **43**, 42-52 (2021)
CoP-NC@NFP	0.72	270	2.85 ± 0.01	*Chem. Eng. J.* **428**, 131115 (2021)
CNT@SAC-Co/NCP	0.74	380	100.00 ± 0.01	*Adv. Funct. Mater.* **31**, 2103360 (2021)
Mn-RuO_2	0.64	270	-	*J. Am. Chem. Soc.* **144**, 2694-2704 (2022)
Co,Nb-MoS_2/TiO_2 HSs	0.7	340	-	*Nano Energy* **82**, 105750 (2021)
Co/CNFs	0.654	320	33.33 ± 0.01	*Adv. Mater*. **31**, 1808043 (2019)

NiFe-LDH Co,N-CNF	0.752	312	83.33 ± 0.01	*Adv. Energy Mater.* **7**, 1700467 (2017)
Co/Co-N-C	0.72	310	10.00 ± 0.01	*Adv. Mater.* **31**, 1901666 (2019)
Co/N-C	0.72	330	33.33 ± 0.01	*Chem. Eng. J.* **433**, 134500 (2022)
ODAC-CoO-30	0.745	364	-	*Adv. Funct. Mater.* **31**, 2101239 (2022)

Table S4. Zn-air batteries performance of some previous literature of nonprecious metal or nonmetal catalysts.

Air catalysts	Open circuit potential/ V	Power density /mW cm^{-2}	Specific capacity /mAh g^{-1}	Durability /h	Reference
Co_{SA}-RuO_2-NUCN	**1.55**	**156.6**	**766.15**	**800**	**This work**
CoNP@FeNC-0.05	1.51	104.4	-	500	*Nano-Micro Lett.* **14**,162 (2022)
$Co(OH)_2$@NC	1.45	34.3	798.3	85	*Small* **17**, e2101720 (2021)
FeS/Fe_3C@NS-C-900	1.455	90.9	750	865	*ACS Appl. Mater. Interfaces.* **12**, 44710-44719 (2022)
Co/CoS/Fe-HSNC-700	1.49	213	747	50	*Appl. Catal., B* **268**, 118729 (2020)
Co/MnO@NC	1.50	146	692	400	*Chem. Eng. J.* **403**, 126385 (2020)
Co@NCNR	1.54	76.76	726	-	*Energy Environ. Mater.* (2022)
Co@IC/MoC@PC	1.395	221	728	100	*ACS Nano* **15**, 13399-13414 (2021)
Co@N-C700	1.41	133	712	240	*Chem. Eng. J.* **421**, 129719 (2021)
CNT@SAC-Co/NCP	1.45	172	864.8	210	*Adv. Funct. Mater.* **31**, 2103360 (2021)
H-Co@FeCo/N/C	1.45	125.2	-	200	*Appl. Catal., B.* **278**, 119259 (2020)
Cop@CoNC	1.46	188.8	791.4	360	*Energy Storage Mater.* **46**, 553-562 (2022)

Co@NiFe-LDH	1.44	165	652	90	*J. Mater. Chem. A* **10**, 5244 (2022)
Co@hNCTs-800	1.45	149	746	500	*Nano Energy* **71**, 104592 (2020)
Co@LCO-NFs	1.43	198	791	200	*J. Mater. Chem. A* **8**, 19946-19953 (2020)
Co@NCW	1.51	47.5	802.7	240	*Appl. Catal., B* **317**,121758 (2022)

References

1. X. Q. Wu, F. Y. Chen, N. Zhang, Y. M. Lei, Y. C. Jin, A. Qaseem and R. L. Johnston, *Small*, 2017, **13**, 1603387.
2. J. Liu, X. Meng, J. H. Xie, B. Liu, B. Tang, R. Y. Wang, C. Wang, P. Gu, Y. D. Song, S. C. Huo, and J. L. Zou, *Adv. Funct. Mater.,* 2023, **33**, 2300579.
3. R. Y. Wang, J. Liu, J. H. Xie, Z. Cai, Y. Yu, Z. X. Zhang, X. Meng, C. Wang, X. Q. Xu, J. L. Zou, *Appl. Catal., B*, 2023, **324**, 122230.
4. H. Jiang, J. Gu, X. Zheng, M. Liu, X. Qiu, L. Wang, W. Li, Z. Chen, X. Ji and J. Li,, *Energy Environ. Sci.*, 2019, **12**, 322.
5. K. Liu, C. Zhang, Y. Sun, G. Zhang, X. Shen, F. Zou, H. Zhang, Z. Wu, E. Wegener, C. Taubert, J. Miller, Z. Peng and Y. Zhu, *ACS Nano*, 2018, **12**, 158-167.
6. G. He, M. Qiao, W. Li, T. Zhao, R. Zou, B. Li, J. Darr, J. Hu, M. Titirici and I. Parkin, *Adv. Sci.,* 2017, **4**, 1600214.
7. X. Han, W. Zhang, X. Ma, C. Zhong, N. Zhao, W. Hu and Y. Deng, *Adv Mater.*, 2019, **31**, 1808281.
8. B. Zhang, C. Zhu, Z. Wu, E. Stavitski, Y. Lui, T. Kim, H. Liu, L. Huang, X. Luan, L. Zhou, K. Jiang, W. Huang, S. Hu, H. Wang and J. Francisco, *Nano Lett.*, 2020, **20**, 136-144.
9. Q. Zhou, Z. Zhang, J. Cai, B. Liu, Y. Zhang, Z. Wang, *Nano Energy*, 2020, **71**, 104592.
10. S. Li, C. Cheng, X. Zhao, J. Schmidt, A. Thomas and Shuang Li, *Angew. Chem*., 2018, **130**, 1874-1880.
11. Y. Tian, X. Liu, L. Xu, D. Yuan, Y. Dou, J. Qiu, H. Li, J. Ma, Y. Wang, D. Su and S. Zhang, *Adv. Funct. Mater.,* 2021, **31**, 2101239.
12. Z. Wu, X. Lu, S. Zhang and X. Lou, *Adv. Funct. Mater.*, 2020, **30**, 1910274.

13.Y. Guo, J. Zhang, H. Xia, M. Zhou, J. Li, Y. Qiao and Q. Xu, *Adv. Funct. Mater.*, 2018, **28**, 1805641.

14. H. Li, J. Wang, R. Qi, Y. Hu, J. Zhang, H. Zhao, J. Zhang and Y. Zhao, *Appl. Catal., B*, 2021, **285**, 119778.

15. J. Sun, S. Lowe, L. Zhang, Y. Wang, K. Pang, Y. Wang, Y. Zhong, P. Liu, K. Zhao, Z. Tang and H. Zhao, *Angew. Chem., Int. Ed*., 2018, **57**, 16511.